GRADUATE AERONAUTICAL LABORATORIES
CALIFORNIA INSTITUTE OF TECHNOLOGY

Mixing in turbulent jets: scalar and isoscalar measures

H. J. Catrakis and P. E. Dimotakis

GALCIT Report FM95-3
5 July 1995

Firestone Flight Sciences Laboratory

Guggenheim Aeronautical Laboratory

Karman Laboratory of Fluid Mechanics and Jet Propulsion

Pasadena

Mixing in turbulent jets: scalar and isoscalar measures

H. J. Catrakis and P. E. Dimotakis

Graduate Aeronautical Laboratories
California Institute of Technology
Pasadena, CA 91125

Experiments have been conducted to investigate mixing and the geometry of isosurfaces in turbulent jets. Specifically, we have obtained high-resolution, high-signal-to-noise-ratio images of the jet-fluid concentration in the far-field of round, liquid-phase, turbulent jets, in the Reynolds number range $4.5\times10^3 \leq Re \leq 18\times10^3$, using laser-induced-fluorescence techniques. Analysis of these data shows that this Reynolds-number range spans a mixing transition in the far field of turbulent jets. This is manifested in the probability-density function of the scalar field as well as in measures of the scalar isosurfaces. Classical as well as fractal measures of the isosurfaces were computed, from small to large scales, and found to be functions of both scalar threshold and Reynolds number, indicating a transition between different turbulent-mixing regimes. The coverage of level sets of concentration in the two-dimensional images was found to possess a scale-dependent-fractal dimension that increases continuously with increasing scale, from near unity, at the smallest scales, to 2, at the largest scales. The geometric complexity of the isosurfaces, therefore, is not self-similar but instead increases with increasing scale. Such behavior necessitates a scale-dependent generalization of fractal geometry. Additional evidence in a variety of other natural phenomena also supports this scale-dependent-fractal extension.

5 July 1995

Introduction

In the turbulent-jet mixing of a passive scalar (jet-fluid concentration), the surfaces of constant mixed-fluid concentration, or scalar isosurfaces, have been demonstrated to be complex, *e.g.*, Dimotakis, Miake-Lye, & Papantoniou (1983). Knowledge of the geometry of such isosurfaces is necessary for an understanding of turbulent-mixing processes. In particular, molecular mixing occurs across such surfaces; in the case of hydrocarbon combustion, chemical reactions are largely confined to the instantaneous (isoscalar) stoichiometric surface. Isosurface measures, such as surface-to-volume ratio or volume-fill fraction, are, as a consequence, important to our understanding and modeling of mixing, chemical reactions, and combustion in turbulent flows.

The characterization of the geometry of isosurfaces in turbulence, in particular, and of complex natural phenomena, in general, requires extending notions of Euclidean geometry. One such extension was proposed by Mandelbrot (1967, 1975b, 1977, 1983) who suggested that fractional (non-integer) dimensions can be used to describe complex geometries in Nature. The word *fractal* was coined by Mandelbrot (1975a,b) to denote geometric objects that are characterized by constant and, in general, fractional dimensions. Such objects are "rough and fragmented to the same degree at all scales" (Mandelbrot 1989). Fractal geometry has been applied to the description of a wide variety of natural phenomena (*e.g.*, Mandelbrot 1983). In these descriptions, fractals are used to characterize the geometry in a finite range of scales that is bounded by upper and lower cutoff length scales, "a property we can assume for all objects arising as a result of any physical process" (Vicsek 1992). The underlying point of view, in all proposed descriptions of natural objects as fractals, is that "over certain ranges of scale they appear very much like fractals and at such scales may usefully be regarded as such" (Falconer 1990). Fluid turbulence, a phenomenon long recognized to possess complex spatial structure, was considered by Mandelbrot (1975a,b) as a candidate for a power-law fractal-geometry description.

In this paper, we investigate mixing and the geometry of isosurfaces in turbulent jets. Both classical and fractal measures are analyzed for the isosurfaces. Reynolds number as well as scalar-threshold dependence is found for both types

of measures. Our findings necessitate an extension of fractal ideas that can accommodate the complex geometries occurring in turbulence and other natural phenomena, for which power-law fractal descriptions cannot capture various geometric measures. We argue that, in general, natural phenomena may be expected to exhibit scale-dependent-fractal behavior and present experimental evidence of scale-dependent-fractal behavior in turbulent mixing. Additional evidence in a variety of other natural phenomena also supports the proposed extension. Finally, we discuss examples of geometric measures that can be computed within the context of scale-dependent-fractal geometry.

Experiments

We have conducted experiments in liquid-phase, turbulent-jet flows and have obtained images of slices through the three-dimensional scalar far-field of round, turbulent jets. A schematic of the flow facility and diagnostics is shown in Fig. 1. Transverse sections of the jet, at a downstream station $z/d = 275$, where $d = 2.54$ mm is the jet-nozzle diameter, were imaged on a cryogenically-cooled, (1024×1024)-pixel, CCD camera (Photometrics Series 200 system), using planar, laser-induced fluorescence. A window at the bottom of the tank provided optical access and a 45° mirror facilitated imaging from underneath the tank. The jet plenum was seeded with fluorescent dye (disodium fluorescein) at a concentration of $c_0 \simeq 2.0 \times 10^{-6}$ M. At the downstream station used for these experiments ($z/d = 275$), the low plenum dye concentration resulted in a scalar fluorescent dye field with negligible laser attenuation across the field of view. The field of view spans approximately 42 cm, resulting in a pixel resolution of $\lambda_p \simeq 420$ μm, and contains the full transverse spatial extent of the turbulent-jet fluid at the measuring station. A beam from a continuous Argon-ion laser (Coherent Innova 90), collimated by a long focal-length spherical lens to a waist size smaller than the pixel resolution and synchronized with the camera shutter, was swept across the jet using a small-inertia, galvanometrically-driven, linearly-scanned mirror. Background laser light was filtered out using a low-pass optical filter (Kodak No. 22). The experiments were conducted in a dark environment to minimize noise due to ambient light. More information on the

facility, including the flow-management system, can be found in Miller & Dimotakis (1991a) and references therein.

Figure 2 shows a schematic of the geometry of the scalar far field of the jet and the imaging station. The laser-illumination sheet was at constant z/d, *i.e.*, in the similarity plane of the jet, and spanned the entire extent of the scalar field at that downstream location. The laser-induced fluorescence-image data were processed using a pixel-by-pixel calibration of the CCD array for noise, sensitivity, and laser illumination variations in the field of view. Each raw fluorescence-data image, $I_{\rm raw}(x,y)$, was calibrated and normalized with an ensemble-average of four background-noise images and four uniform-concentration images recorded for each run condition, *i.e.*,

$$\frac{c(x,y;z=\text{const})}{c_{\rm ref}} \;=\; \frac{I_{\rm raw}(x,y) \;-\; \langle I_{\rm bck}(x,y)\rangle}{\langle I_{\rm ill}(x,y)\rangle \;-\; \langle I_{\rm bck}(x,y)\rangle} \quad , \tag{1}$$

where $c_{\rm ref}$ is a reference concentration which is constant for all runs. The background-noise images, $I_{\rm bck}(x,y)$, were recorded shortly before each run with no dye in the tank. Each such image was recorded at the same location as the (raw) jet images, along the same optical path, with the camera shutter open for the same exposure time as for the jet images. After the jet-plenum fluid had completely discharged into the tank, all of the water and dye was recirculated continuously in the tank. During the recirculation process, the laser-induced fluorescence at the imaging station was monitored for non-uniformities of the dye concentration in the plane of illumination. After a sufficiently long time, non-uniformities were no longer visible and images corresponding to a uniform-concentration field were recorded and used to measure the illumination distribution in the field of view, $I_{\rm ill}(x,y)$, as well as provide a jet-fluid concentration reference. The procedure of emptying all the jet-plenum fluid into the tank allowed the computation of the local scalar values, $c(x,y)$, to be referenced, in absolute value, to the (pure) jet-plenum concentration, c_0, for all runs, *i.e.*,

$$\frac{c(x,y)}{c_0} \;=\; \frac{c(x,y)}{c_{\rm ref}}\,\frac{c_{\rm ref}}{c_0} \;=\; \frac{c(x,y)}{c_{\rm ref}}\,\frac{V_{\rm plenum}}{V_{\rm tank}\,+\,V_{\rm plenum}} \;\simeq\; \frac{c(x,y)\,/\,c_{\rm ref}}{2.2\times 10^2} \quad , \tag{2}$$

where $V_{\rm plenum} \simeq 5.0\times 10^{-3}$ m^3 is the plenum volume and $V_{\rm tank} \simeq 1.1$ m^3 is the tank volume.

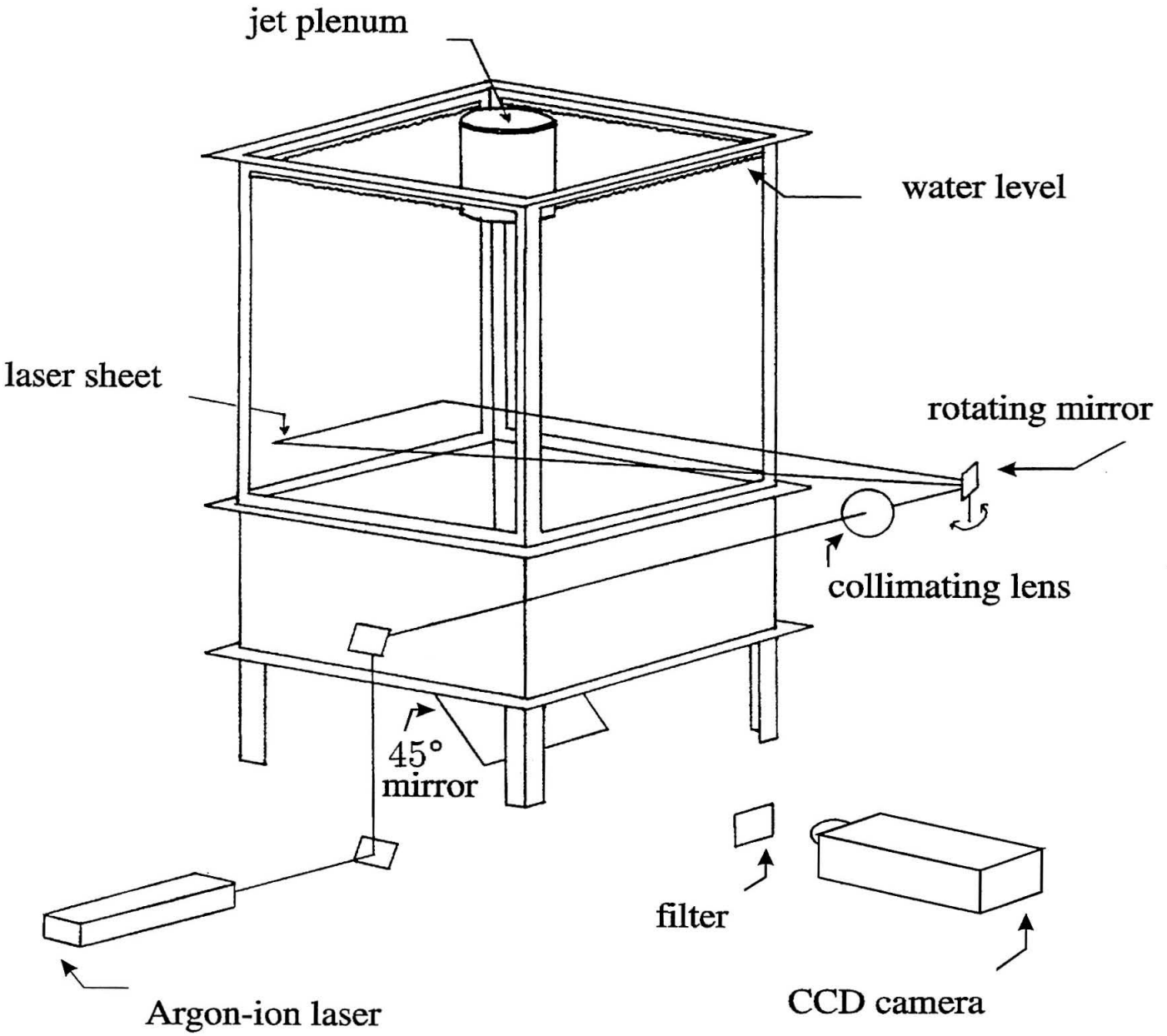

FIG. 1 Flow facility and diagnostics schematic

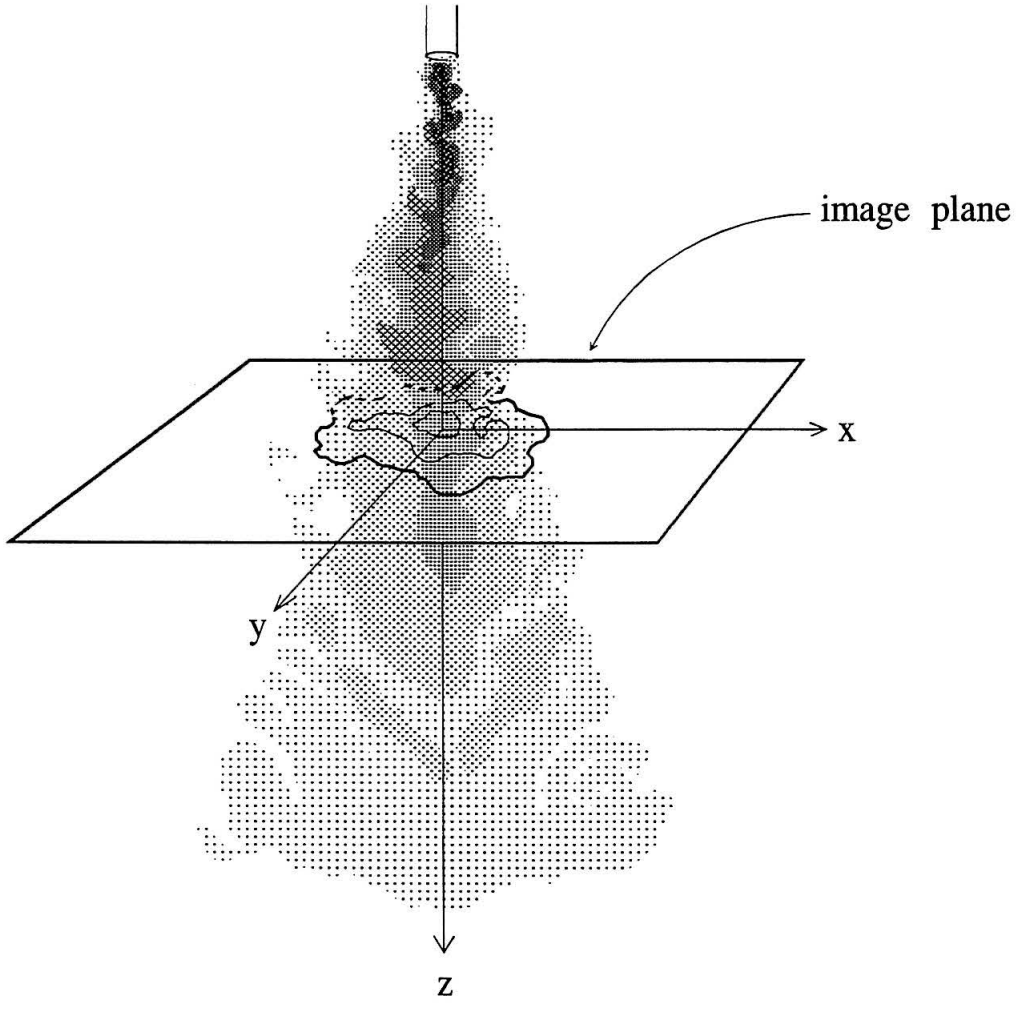

FIG. 2 Jet scalar far-field geometry and image plane schematic.

The jet Reynolds number was varied in this investigation in the range $4.5 \times 10^3 \leq Re \leq 18 \times 10^3$. For round, turbulent jets, at a downstream distance z, $Re \equiv u(z)\,\delta(z)/\nu$, where $u(z) \propto 1/z$ is the local jet centerline velocity, $\delta(z) \propto z$ is the local jet transverse extent (diameter), and Re is independent of the downstream coordinate. Examples of turbulent-jet scalar-image data at $Re \simeq 4.5\times10^3$, 9.0×10^3, and 18×10^3, normalized and calibrated, are depicted in Figs. 3a-c. For this flow, $Re \simeq Re_0$, where Re_0 is the Reynolds number based on jet-nozzle values, *i.e.*, $Re_0 \equiv u_0\, d\,/\nu$. The jet-fluid field is fully contained within the field-of-view boundaries of

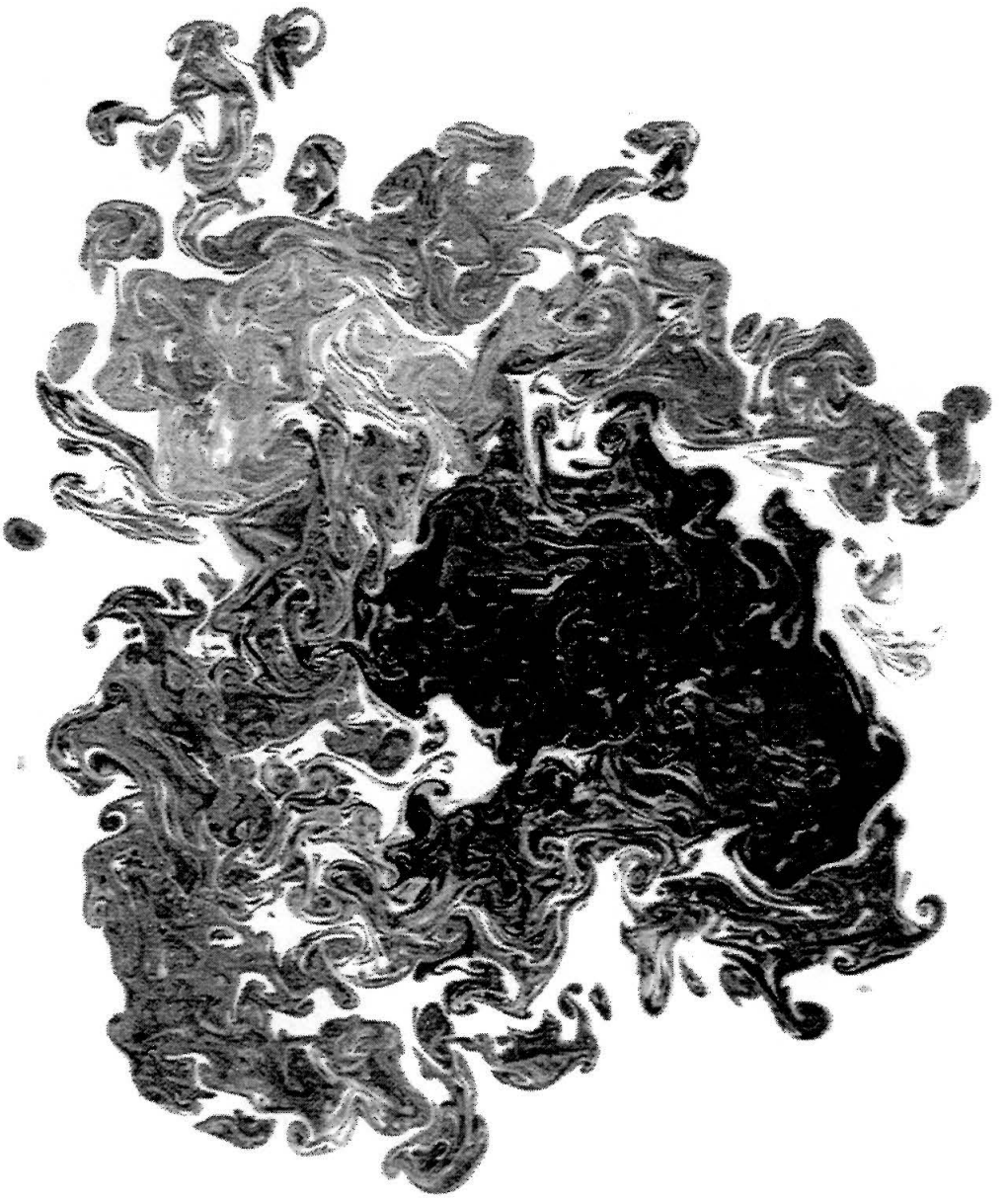

FIG. 3 Jet-fluid concentration in the far-field ($z/d = 275$) of a turbulent jet. (a) $Re \simeq 4.5 \times 10^3$.

the images. Throughout the Reynolds number range investigated, the image field of view was the same. At a Reynolds number of $Re \simeq 9.0 \times 10^3$ (*cf.* Fig. 3b), scalar

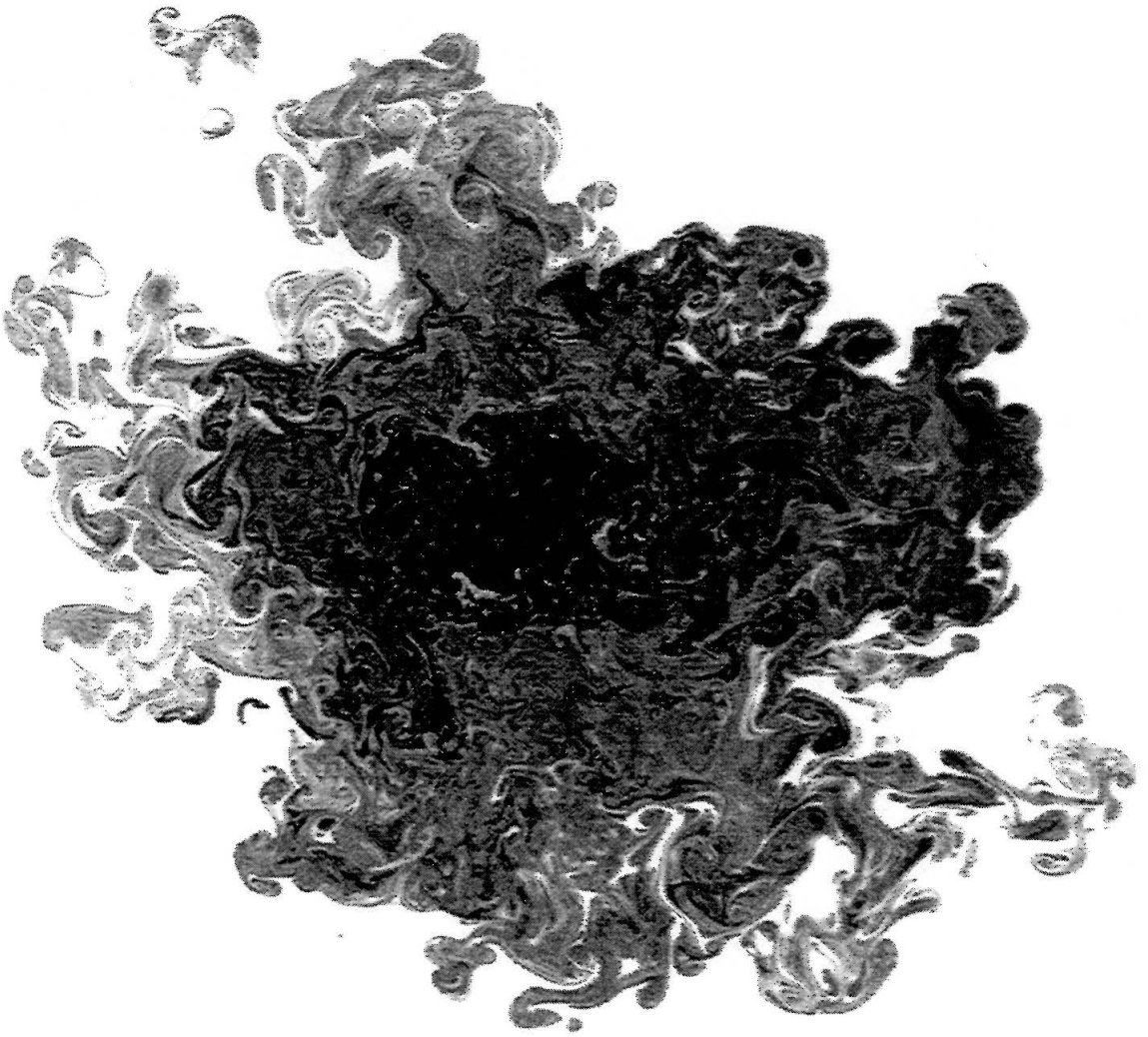

FIG. 3 (b) $Re \simeq 9.0 \times 10^3$.

diffusion-layer thicknesses on the jet centerline are estimated to be approximately half the pixel resolution, and much larger than the pixel resolution near the outer region of the jet where we have focused our investigations.

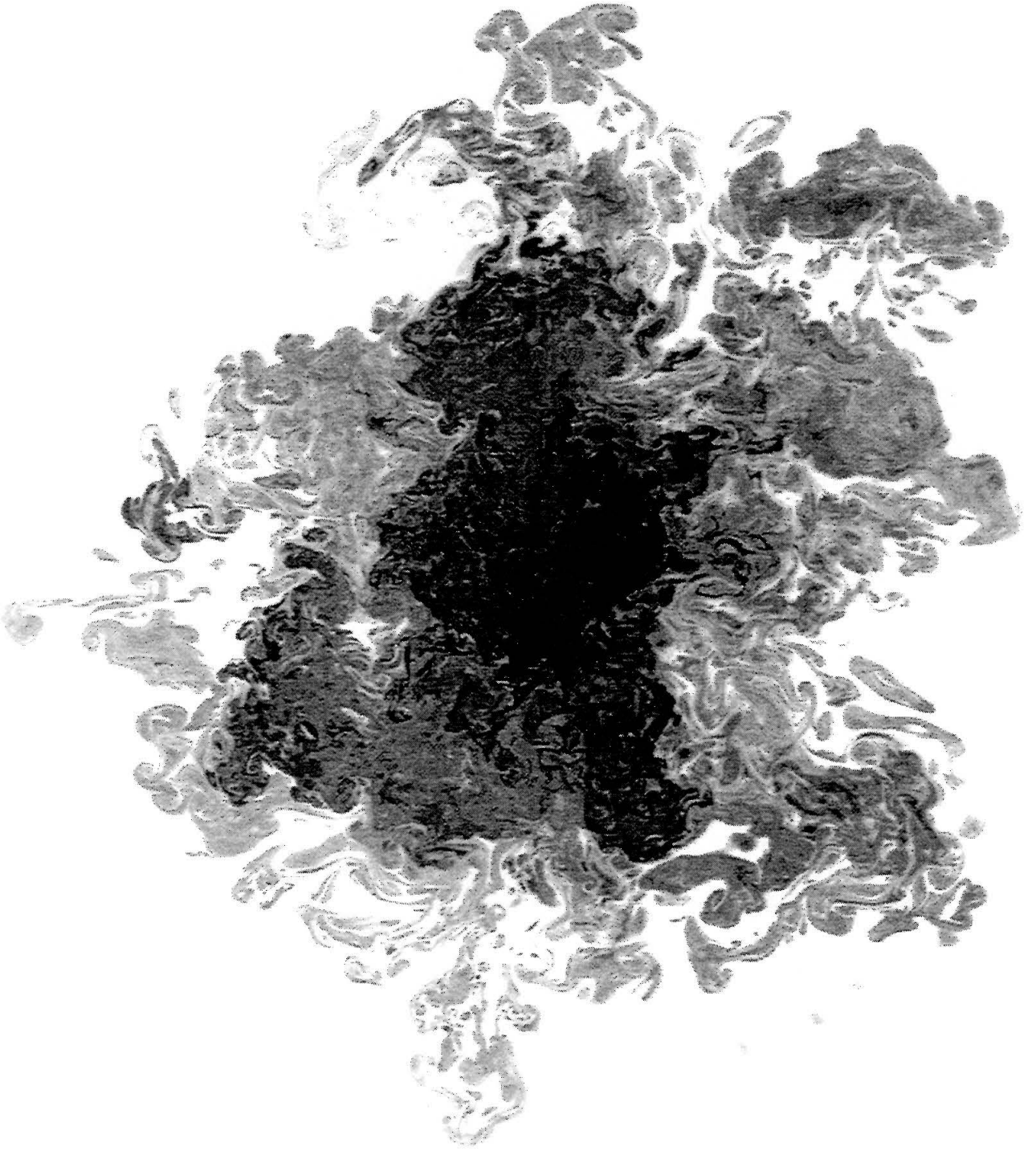

FIG. 3 (c) $Re \simeq 18 \times 10^3$.

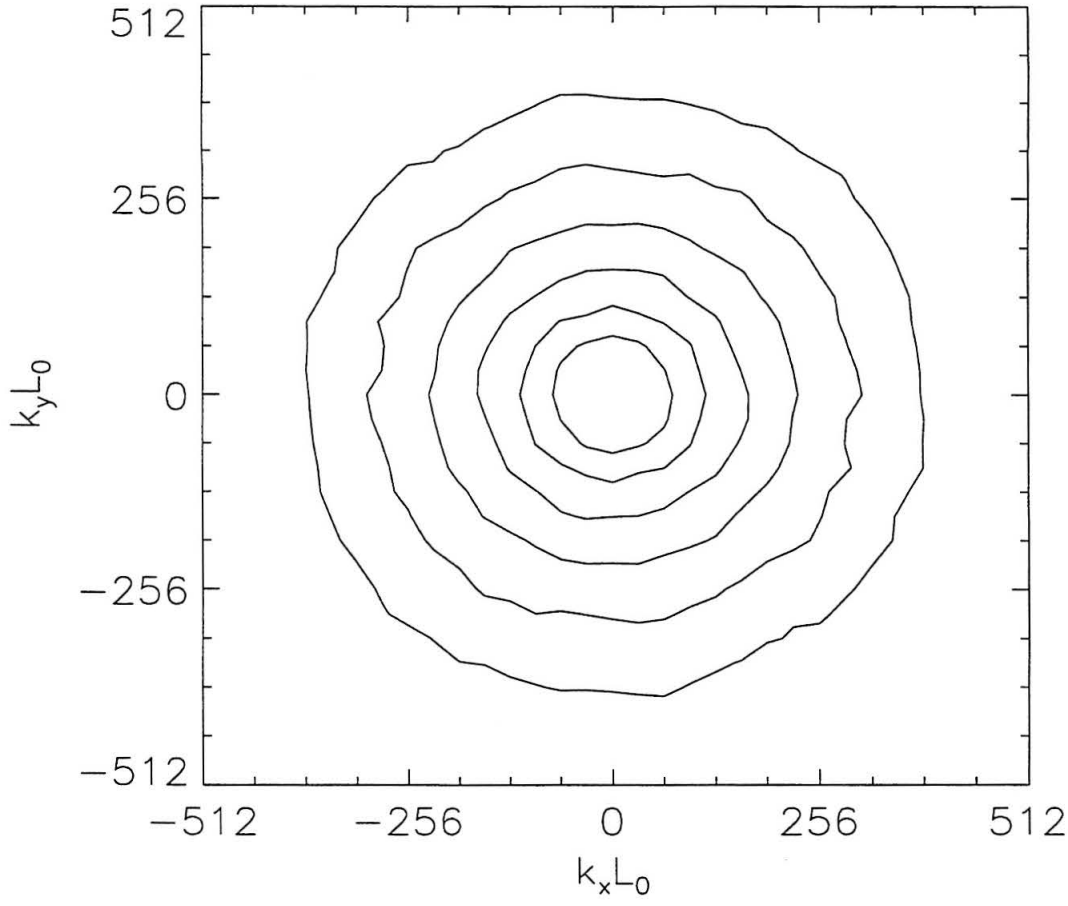

FIG. 4 Contour plot of the (decimal) logarithm of the two-dimensional scalar power spectrum computed from the data depicted in Fig. 3b. Contour values range from -8.5 to -6.0 (outer to inner) in increments of 0.5, in units of $\log_{10}\left(c_{\mathrm{ref}}^2/\lambda_{\mathrm{p}}\right)$. L_0 is the field-of-view scale and λ_{p} is the pixel-resolution scale, with $L_0/\lambda_{\mathrm{p}} = 1024$.

The two-dimensional, scalar power spectrum for the image data of Fig. 3b is shown as a contour plot in Fig. 4. Contours of the scalar power spectrum are seen to be approximately circular. The radial scalar power spectrum, *i.e.*, *vs.* $k = \sqrt{k_x^2 + k_y^2}$, computed from the image data of Fig. 3b, estimated by an azimuthal integration of the two-dimensional power spectrum of Fig. 4, is shown in

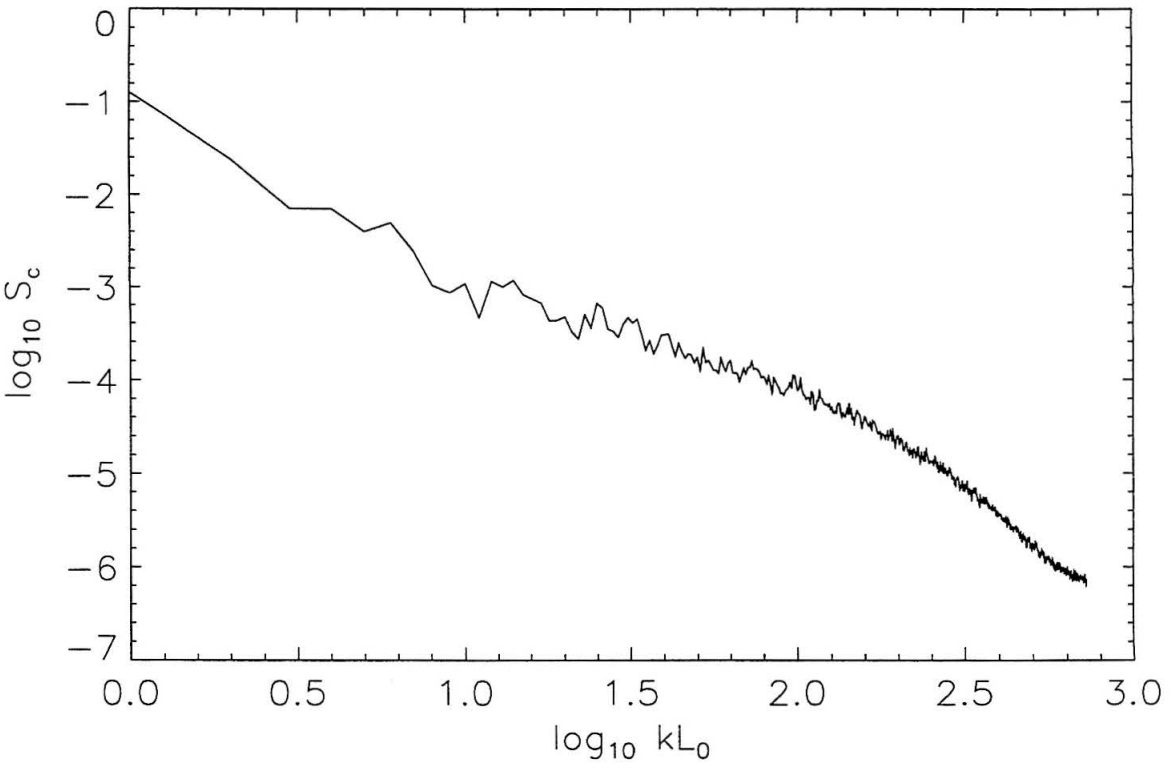

FIG. 5 Radial scalar power spectrum of the image data of Fig. 3b (*cf.* Fig. 4).

Fig. 5. The dynamic range of the scalar-field image data of Fig. 3b can be seen to be, approximately, 50 dB, corresponding to a signal-to-noise (amplitude) ratio of 300:1. Ensemble-averaged, radial power spectra for the three Reynolds numbers investigated are shown in Fig. 6. The ensemble averaged spectra in Fig. 6 were computed from six individual-image realizations at $Re \simeq 9.0 \times 10^3$, three realizations at $Re \simeq 4.5 \times 10^3$, and three realizations at $Re \simeq 18 \times 10^3$. At high wave numbers, the scalar power spectra are seen to decrease with increasing Reynolds number. This behavior of the power spectrum is consistent with the decreasing scalar variance with increasing Reynolds number documented previously for temporal scalar fluctuation measurements in turbulent jets (Miller & Dimotakis 1991b).

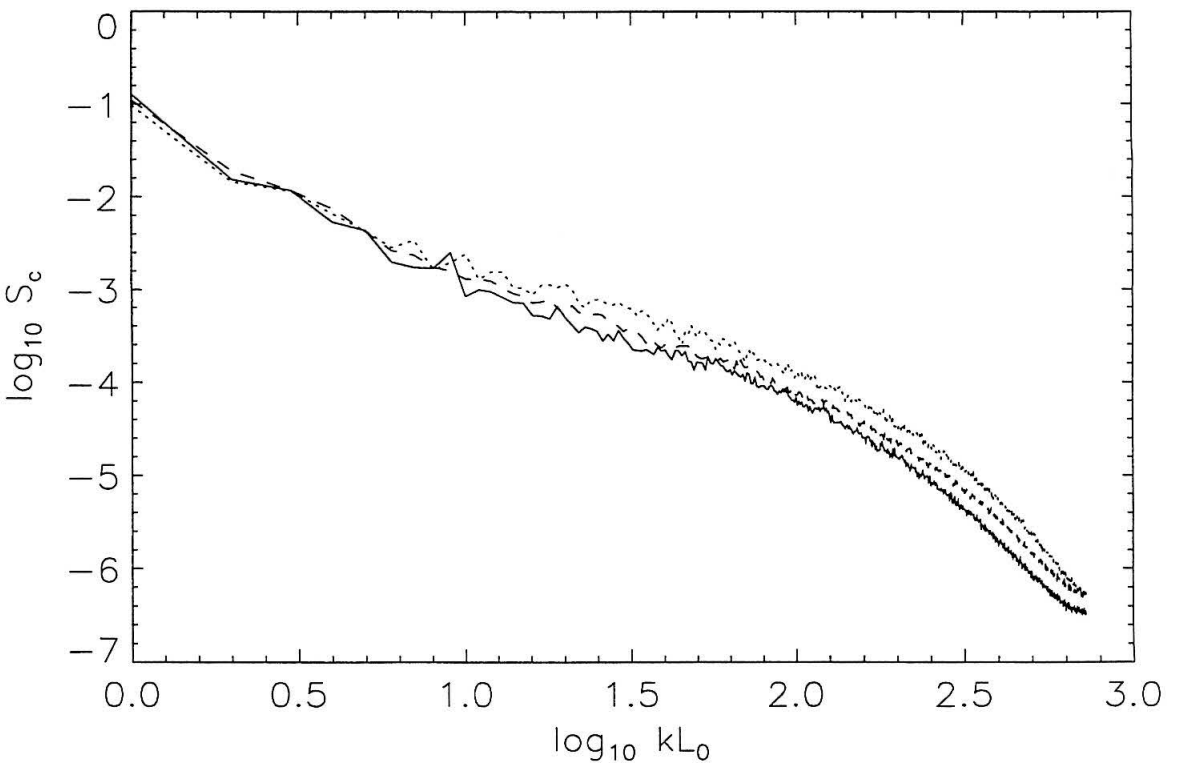

FIG. 6 Ensemble-averaged radial scalar power-spectra. Dotted line: $Re \simeq 4.5 \times 10^3$; dashed line: $Re \simeq 9.0 \times 10^3$; solid line: $Re \simeq 18 \times 10^3$.

Classical scalar and isoscalar measures

The jet-fluid-concentration probability-density functions (pdf), estimated as histograms of the scalar values, are shown in Fig. 7 for $4.5 \times 10^3 \leq Re \leq 18 \times 10^3$. These were computed from ensemble-averaged histograms of six scalar images for $Re \simeq 9.0 \times 10^3$, and from three scalar images for $Re \simeq 4.5 \times 10^3$ and $Re \simeq 18 \times 10^3$. The scalar values are normalized by a constant reference concentration, c_{ref}, where $c_{\mathrm{ref}}/c_0 \simeq 2.2 \times 10^2$ (*cf.* Eq. 2). Low scalar values in Fig. 7 are generally encountered in the outer portion of the images (tank fluid), while high values are encountered in the interior of the images (near the jet centerline, *cf.* Fig. 3). Figure 7 shows that, in the Reynolds number range investigated, the shape of the scalar pdfs changes qualitatively with increasing Reynolds number; the peak of the mixed-fluid concentration pdf shifts to lower values. The pdf values depicted in Fig. 7 are normalized over the field-of-view, which is the same for all images. Figure 7 shows

that the peak of the pdfs increases with increasing Reynolds number. This implies that the jet-fluid concentration scalar field encompasses a larger fraction of area with increasing Reynolds number. The change in the nature of the scalar pdf with increasing Reynolds number, evident in Fig. 7, occurs in the same range of Reynolds numbers which has been documented to produce a mixing transition to fully-developed turbulence in jets and other flows (Dimotakis 1993).

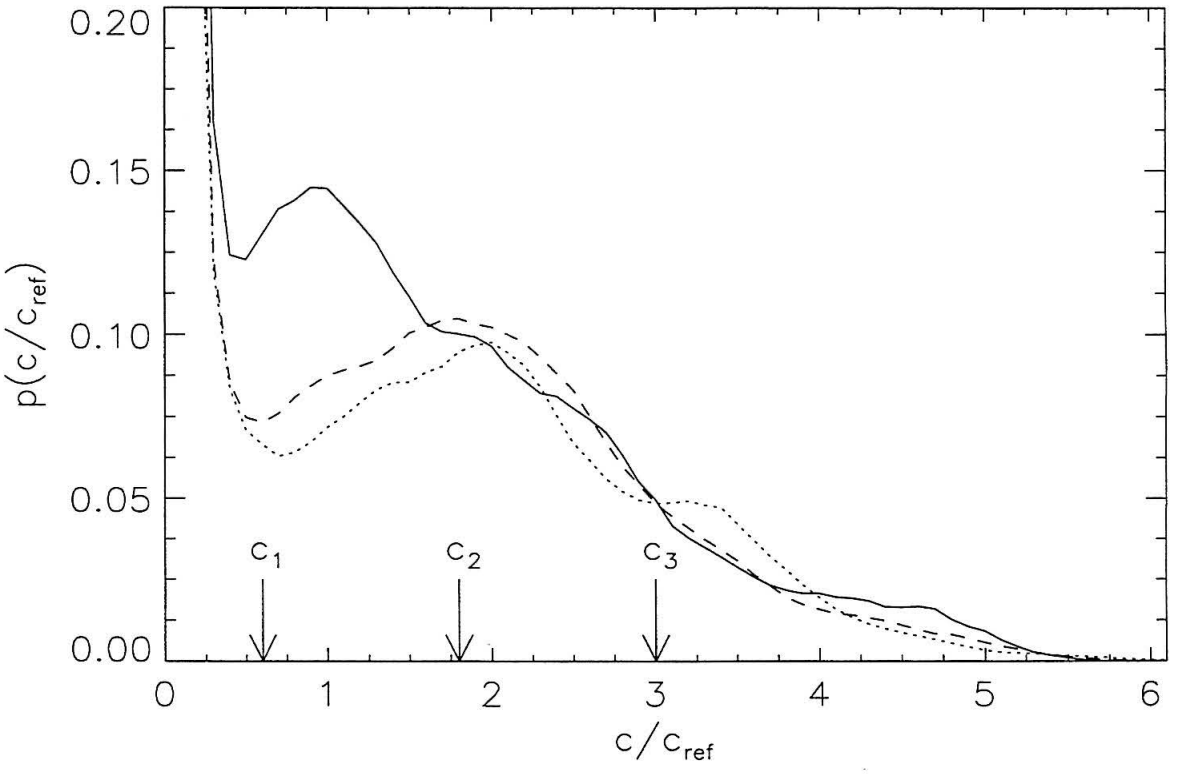

FIG. 7 Jet-fluid concentration pdf in the far-field ($z/d = 275$) of a turbulent jet as a function of Reynolds number, for $4.5 \times 10^3 \leq Re \leq 18 \times 10^3$. Dotted line: $Re \simeq 4.5 \times 10^3$, dashed line: $Re \simeq 9.0 \times 10^3$, solid line: $Re \simeq 18 \times 10^3$. Three scalar-threshold values, c_1, c_2, and c_3, are also indicated.

The scalar pdfs depicted in Fig. 7 imply that isosurface measures are threshold- and Reynolds-number dependent. In the subsequent analysis, three representative thresholds have been chosen at which Reynolds-number comparisons are made. These values are $c_1/c_{\text{ref}} = 0.6$, $c_2/c_{\text{ref}} = 1.8$, and $c_3/c_{\text{ref}} = 3.0$, as indicated in Fig. 7. The medium threshold, c_2, was chosen to correspond to the peak of the $Re =$

9.0×10^3 *pdf.* The lowest threshold, c_1, corresponds to the outer isosurfaces and the highest threshold, c_3, corresponds to the tails of the pdfs, for all Reynolds numbers in the range investigated. Examples of outer isosurfaces of jet-fluid concentration for $4.5 \times 10^3 \leq Re \leq 18 \times 10^3$ at scalar threshold $c = c_1$ (*cf.* Fig. 7) are shown in Figs. 8a-c, superimposed on the image data of Fig. 3 from which they are derived. Isosurfaces of jet-fluid concentration were constructed from the recorded scalar-image data using bilinear interpolation and are depicted, in Fig. 8, using boundary-outline pixels (*cf.* Appendix).

The area enclosed by the scalar level sets, normalized by the square of the distance downstream, A/z^2, is shown in Fig. 9 as a function of scalar threshold and Reynolds number. This was computed by summing the area of all regions with scalar value larger-than-or-equal-to the threshold. For the computation of this area, the isosurfaces were represented using bilinear interpolation (*cf.* Appendix). The area enclosed by the outer isosurfaces, at a given threshold, is seen to increase with increasing Reynolds number. Also, this behavior is seen to occur in a range of lower thresholds that diminishes with increasing Reynolds number. The outer isosurfaces are associated with lower velocities than the inner isosurfaces, *i.e.*, locally more viscous, and can be expected to be more sensitive to changes in Reynolds number.

The identification of scalar isosurfaces (*cf.* Fig. 8) allows the local jet diameter to be estimated. A measure of the isoscalar spatial extent can be computed by identifying the smallest *circumscribing rectangle* (*cf.* Tricot 1995) that covers each isosurface. Figure 10 shows an example of a circumscribing rectangle identified for the isosurface of Fig. 8, as well as the extent of the field-of-view of the image. The isoscalar spatial extent based on this circumscribing rectangle, δ_{r}, was computed as the square root of the area of the rectangle, *i.e.*,

$$\delta_{\mathrm{r}} \equiv (\lambda_x \lambda_y)^{1/2} \quad , \tag{3}$$

where λ_x and λ_y are the lengths of the two sides of the circumscribing rectangle (*cf.* Eq. A.1). Figure 11 shows the ensemble-averaged spatial extent, normalized by the distance downstream, δ_{r}/z, as a function of scalar threshold and Reynolds number. As expected, the isoscalar spatial extent decreases monotonically with increasing scalar threshold at a given Reynolds number. There is a qualitative

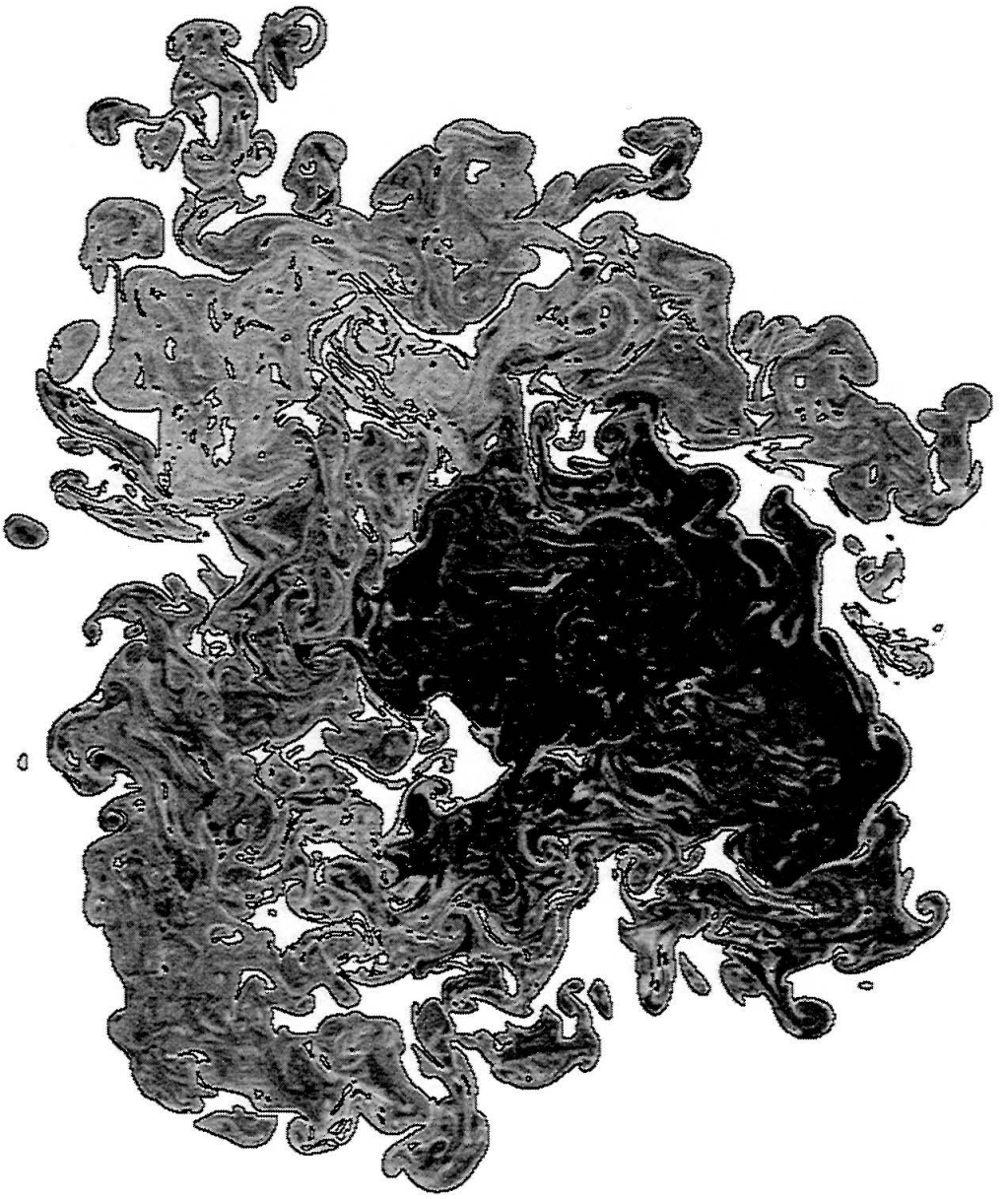

FIG. 8 Outer level set of jet-fluid concentration in the far-field of a turbulent jet, at scalar threshold $c = c_1$, superimposed on the image data of Fig. 3 and depicted using boundary-outline pixels (*cf.* Appendix). (a) $Re \simeq 4.5 \times 10^3$.

change in the behavior of δ_r with c/c_{ref}, however, as the Reynolds number changes

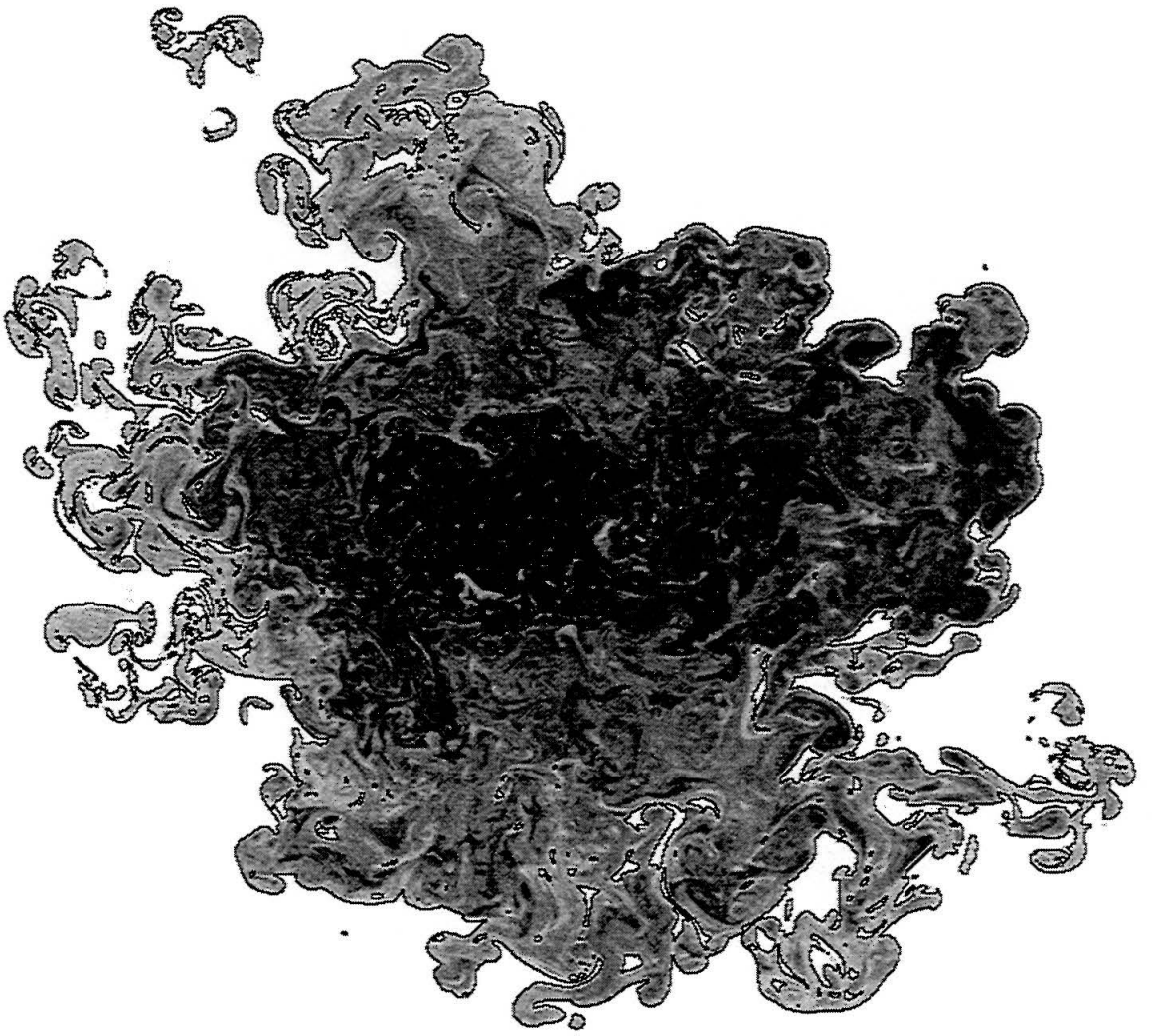

FIG. 8 (b) $Re \simeq 9.0 \times 10^3$.

from 4.5×10^3 to 18×10^3. The spatial extent of the outer isosurfaces increases with increasing Reynolds number. At the same time, the extent of the inner isosurfaces decreases with increasing Reynolds number. The variation of δ with c/c_{ref} appears

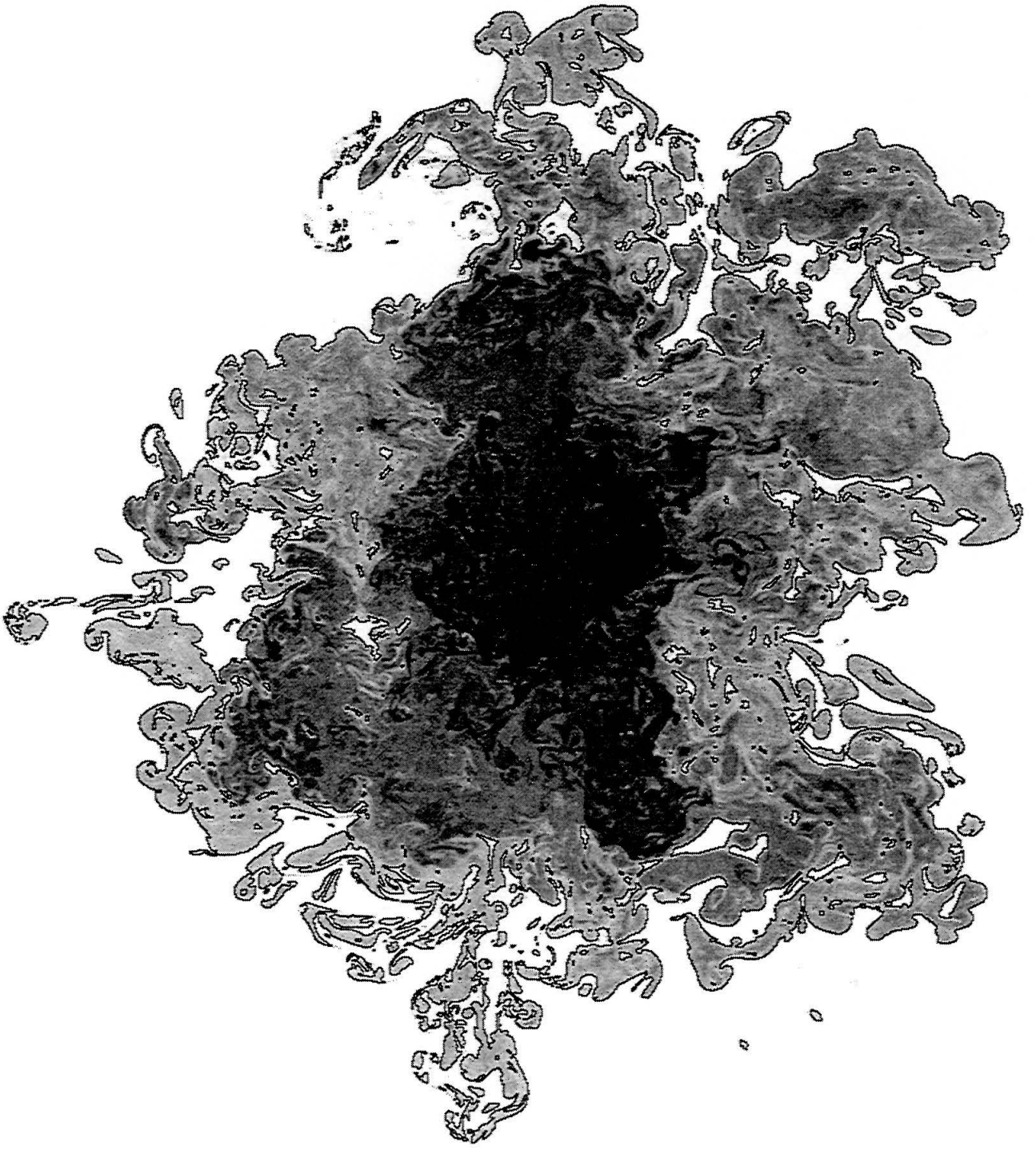

FIG. 8 (c) $Re \simeq 18 \times 10^3$.

to become linear with increasing Reynolds number, indicating an approach to a Re-independent isoscalar spatial extent. This behavior, in addition to the changes in the nature of the scalar pdfs and area enclosed by the level sets noted above, occurs in a range of Reynolds numbers for the mixing transition to fully-developed turbulence in free-shear flows (Dimotakis 1993).

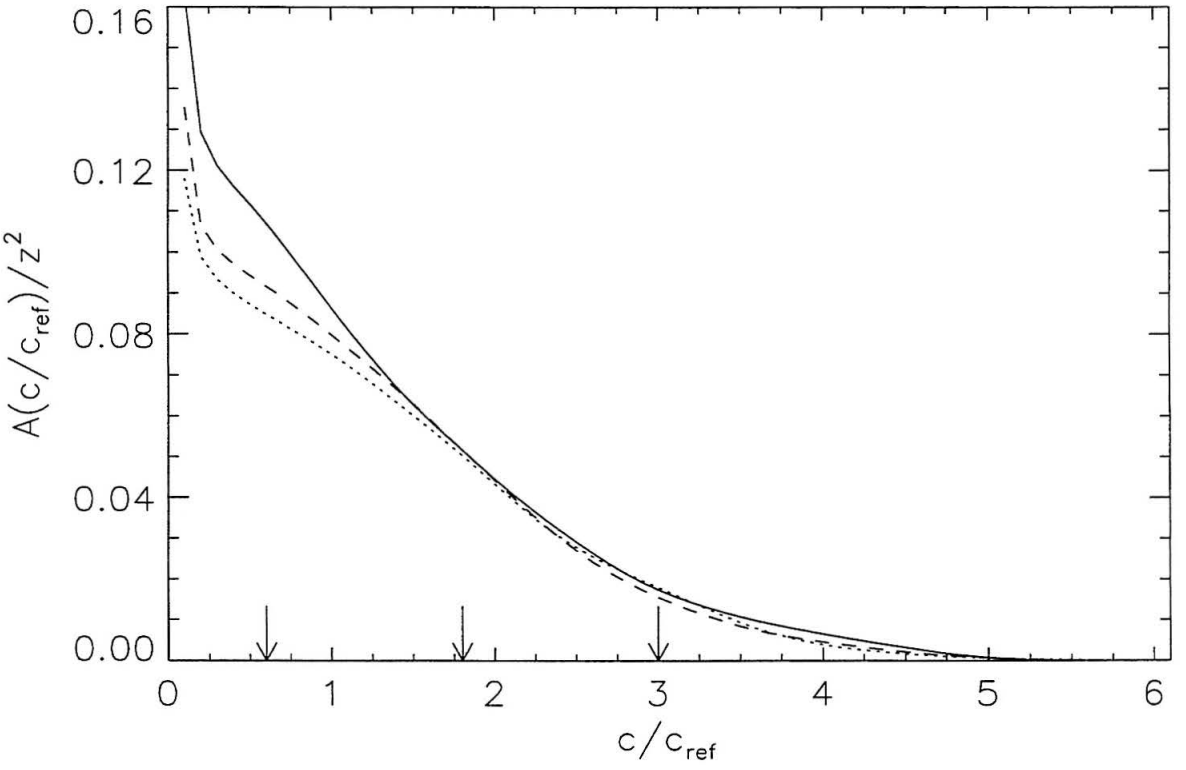

FIG. 9 Area A enclosed by scalar level sets, in the similarity plane of the jet, as a function of scalar threshold and Reynolds number. Dotted line: $Re \simeq 4.5 \times 10^3$, dashed line: $Re \simeq 9.0 \times 10^3$, solid line: $Re \simeq 18 \times 10^3$. Three scalar-threshold values, c_1, c_2, and c_3, are also indicated (*cf.* Fig. 7).

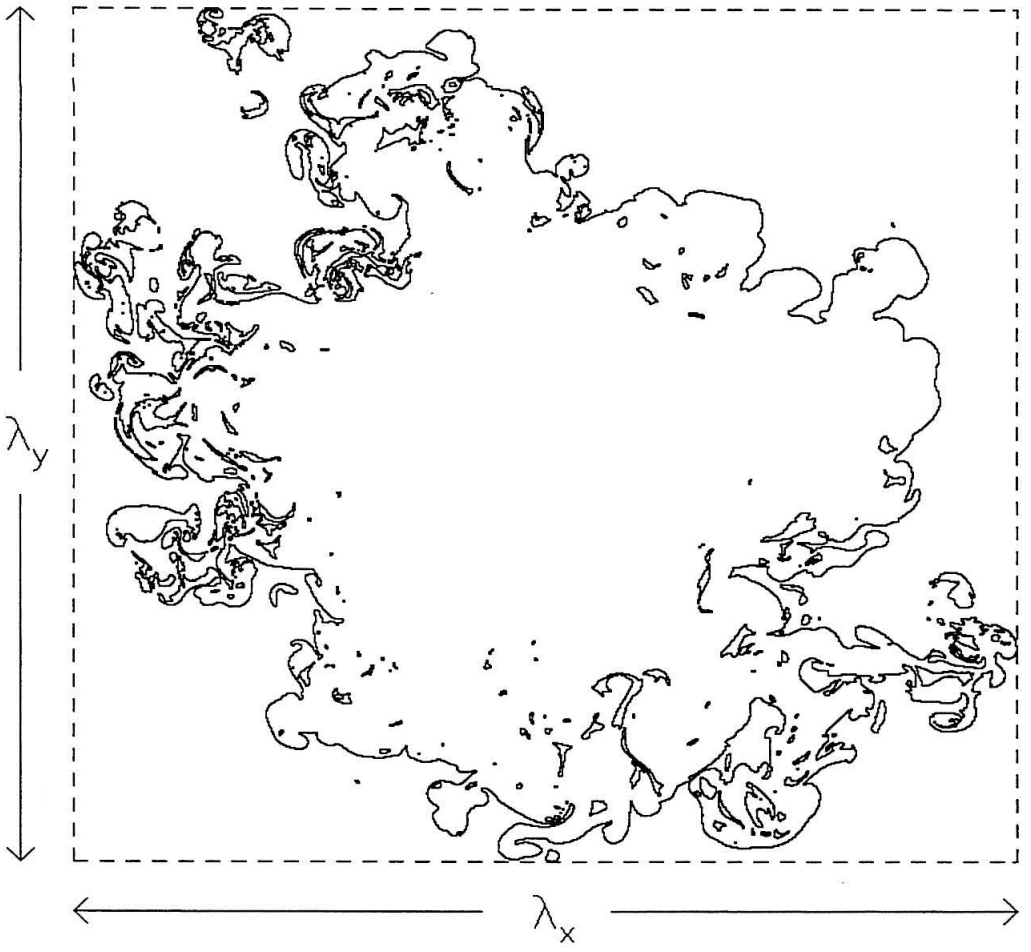

FIG. 10 Circumscribing rectangle (dashed line) for the level set of Fig. 8. Dotted line: field-of-view boundaries.

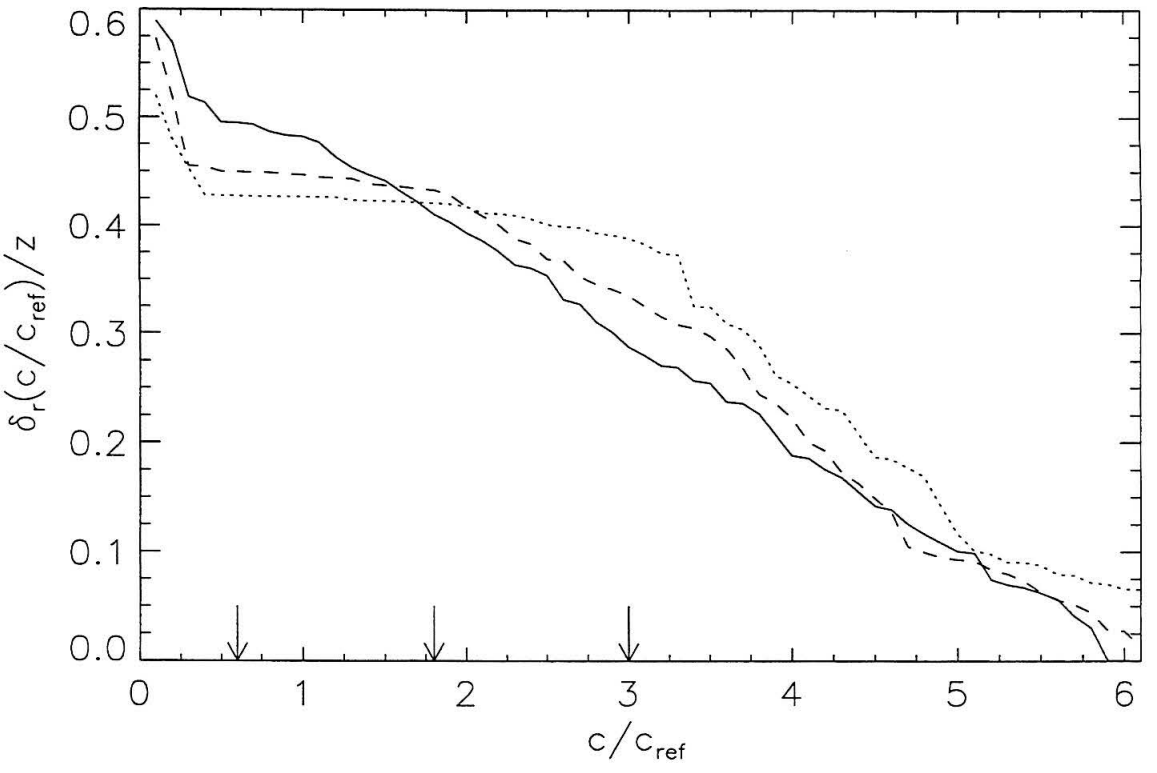

FIG. 11 Isoscalar spatial extent based on circumscribing rectangle, δ_r, as a function of scalar threshold and Reynolds number. Dotted line: $Re \simeq 4.5 \times 10^3$, dashed line: $Re \simeq 9.0 \times 10^3$, solid line: $Re \simeq 18 \times 10^3$. Three scalar-threshold values, c_1, c_2, and c_3, are also indicated (*cf.* Fig. 7).

Fractal geometry

Ever since Richardson's (1961) analysis of data on the length of coastlines and borders between countries and Mandelbrot's (1967) subsequent interpretation, it has become appreciated that complex curves and surfaces have scale-dependent length and area, respectively, that increase as one measures down to smaller and smaller scales. This is a consequence of the presence of ever-finer features that are encountered as the scale of measurement is reduced. Fractal curves have a scale-dependent length, $L(\lambda)$, that increases in a power-law fashion with decreasing scale, λ, *i.e.*,

$$L(\lambda) \propto \lambda^{1-D} \quad , \tag{4}$$

with a dimensional prefactor. Fractal sets exhibit a scale-dependent geometric cov-

erage, $N(\lambda)$, given by the number of elements of size λ needed to cover the set, that follows a power-law, *i.e.*,

$$N(\lambda) \propto \lambda^{-D} \quad , \tag{5}$$

also with a dimensional prefactor. Power-law geometric-coverage relations, such as Eq. 5, constitute scaling laws that are scale-independent. From such power-law relations, the fractal dimension is identified with the scaling exponent, *i.e.*,

$$D = -\frac{\mathrm{d}\log N(\lambda)}{\mathrm{d}\log \lambda} \ . \tag{6}$$

The fractal dimension, D, of Eq. 6, is a constant only when the coverage, $N(\lambda)$, follows an exact power-law. Constant fractal dimensions, in other words, apply only to geometric structures that exhibit scale-independent behavior.

Mandelbrot (1975a,b) proposed that fractal geometry may be applicable to turbulence, suggesting a fractal dimension of $D_3 = 8/3$ for scalar isosurfaces in homogeneous turbulence with Kolmogorov-Gauss scaling. In the last ten years, the geometry of isosurfaces in turbulence has been the object of various studies. Several investigators have reported fractal behavior in the geometry of turbulence. Sreenivasan & Meneveau (1986) reported experimental findings of constant, scale-independent, fractal dimensions, $D_1 = 0.32$ and $D_2 = 1.33$, for isosurface measurements in a turbulent jet, from which they argued that $D_3 = 2.33$ for the (three-dimensional) isosurfaces. Sreenivasan, Prasad, Meneveau, & Ramshankar (1989) found $D_2 = 1.36$ for isoscalar jet data with $D_2 = 1.35 \pm 0.05$ as a mean value for various turbulent shear flows and presented theoretical arguments for a value of $D_3 = 7/3$. Prasad & Sreenivasan (1990) obtained three-dimensional data of the scalar isosurfaces in turbulent jets and reported a value of $D_3 = 2.35 \pm 0.04$. A theoretical estimate of $D_3 = 2.5$ was obtained by Constantin (1989, 1990a), later refined to $D_3 = 8/3$ (Constantin, Procaccia, & Sreenivasan 1991, Constantin 1994a,b, and Constantin & Procaccia 1994). A lack of fractal scaling of scalar isosurfaces in the interior of the jet was reported by Sreenivasan (1991, p. 553). Constantin, Procaccia, & Sreenivasan (1991), however, reported fractal scaling in the jet interior, with $D_3 = 2.67$, citing the same isosurface for which Sreenivasan (1991, p. 553) had originally concluded that there was no fractal scaling. In particular, Constantin, Procaccia & Sreenivasan (1991) suggested constant, scale-independent values of

$D_3 = 8/3$ for scalar isosurfaces in the jet interior and $D_3 = 7/3$ for scalar isosurfaces near the jet boundary. Procaccia, Brandenburg, Jensen, & Vincent (1992) pointed out, however, that "the theory [of Constantin *et al.* (1991)] cannot exclude the possibility that the scaling exponent D depends on [the scale] r". Procaccia *et al.* (1992) analyzed isosurfaces of vorticity in three-dimensional homogeneous turbulence, using the direct-numerical-simulation data of Vincent & Meneguzzi (1991), and concluded that "it is impossible to state with confidence that the fractal behavior [of the vorticity isosurfaces] is clear-cut". Lane–Serff (1993) computed fractal dimensions of scalar contours in liquid-phase jet and plume flows and reported a threshold-dependent fractal dimension with a minimum value of $D_2 = 1.23$, computed by fitting a straight line using a least-squares fit. He noted, however, that "there is a distinct curve [in the coverage plots]" but attributed this to "the small range between integral and Kolmogorov scales at the Reynolds numbers of [the] experiments". Flohr & Olivari (1994) analyzed scalar contours in gas-phase turbulent jets and found "constant [fractal] scaling behavior over a wide range [of scales]" with a threshold-dependent fractal dimension exhibiting a maximum value. For the outer scalar interface, they found a mean value of $D_2 = 1.30 \pm 0.05$. Sreenivasan (1994) stated that, for outer scalar isosurfaces of turbulent jets, $D_3 = 2.35 \pm 0.05$ with fractal scaling "over much of the interval between the integral scale and the Kolmogorov scale", while for inner scalar isosurfaces, $D_3 = 2.67 \pm 0.05$, in a scaling range "smaller" than that for outer isosurfaces, indicating the degree of confidence of his results as "fairly certain".

Takayasu (1982) had argued, however, that the behavior of turbulent flow is a function of scale, and that, as a consequence, one may expect descriptions of the geometry of turbulence to require fractal dimensions that are functions of scale and not constant, *i.e.*, scale-dependent fractal (SDF) dimensions. With this motivation, he considered the notion of a SDF dimension, $D(\lambda)$, in characterizing the complexity of the path of a one-dimensional random-walk particle with finite mean-free-path and conjectured the applicability of SDF dimensions to physical phenomena, including turbulent diffusion. It is known that, in random walks with finite (and non-zero) mean-free-path, particles perform correlated, or inertial, random walks (Takayasu 1982) and one can expect the trajectory of such a random-walk particle to possess a SDF dimension. Only in the limit of vanishing (zero) mean-free-path does a

random walk become uncorrelated, or Markovian, with a scale-independent fractal dimension of 2, and then can serve as a model for regular diffusion, or Brownian motion. In fact, in a study of turbulent diffusion, Taylor (1920) had considered a modified random walk in which he allowed for particles with inertia, *i.e.*, a random walk with correlated steps. Taylor's modification of the random walk illustrated the nature of turbulent diffusion as a correlated random walk (McComb 1991).

Miller & Dimotakis (1991a) reported experiments in turbulent jets in which no power-law fractal behavior was found in either point, line, or streak-image measurements of the jet-fluid-concentration field. In particular, they computed a SDF dimension $D_1(\lambda)$ for one-dimensional temporal and spatial data and found it to increase smoothly from 0, at the smallest scales, to 1, at the largest scales. They also reported values of $D_{1+1}(\lambda)$, increasing continuously with scale, from near 1 to almost 2, for streak-image data (one space dimension plus time) in the neighborhood of the axis of turbulent jets. Sreenivasan (1991) commented on the Miller & Dimotakis findings, suggesting they could be attributable to differences between temporal and spatial data. See also Kerstein (1991) for an alternate discussion. Dimotakis (1991) interpreted those data, in the context of dimensional analysis and similarity issues in fractal power-law scaling relations, and argued, generally, that characteristic scales are necessary for power-law fractal scaling (*cf.* Eq. 5), in contrast with accepted proposals. Gluckman, Willaime, & Gollub (1993) conducted experiments in thermal turbulence and found that the isothermal surfaces do not display fractal scaling, while scalar isosurfaces do show a limited range of approximately-fractal scaling.

Scale-dependent-fractal (SDF) geometry

A scale-dependent fractal (SDF) is a geometric object characterized by a scale-dependent-fractal dimension, $D(\lambda)$, where the scale is denoted by λ. SDFs obey general geometric-scaling laws and have a more complex geometric structure than power-law fractals. The latter are, by definition, restricted to scale-invariant complexity. The difference between a constant fractal dimension, D, and a SDF dimension, $D(\lambda)$, can be illuminated by the following point of view on the hierarchy of

complex patterns (Mikhailov & Loskutov 1991). Simple Euclidean objects, such as circles, spheres, have structure only on a certain (large) scale and are associated with the integer-valued embedding (Euclidean) dimension, d_e. This level of complexity can be dubbed Level 1. Fractal objects have a structure which persists on all scales and, hence, are more complex than Level 1 objects; they can be assigned Level 2 in complexity. Level 2 objects are associated with a fractal dimension, D. For the power-law fractal objects, it is the *same structure* which persists on various scales. A higher level of complexity, Level 3, can occur when structures of different complexity are encountered at different scales. Level 3 objects are characterized by a SDF dimension, $D(\lambda)$. SDFs can be seen, therefore, as scale-dependent generalizations of (power-law) fractals.

Several investigators have independently considered the notion of a SDF dimension, using various terms to denote $D(\lambda)$, in a variety of contexts. Some of these investigators have also considered SDFs, for which they have employed varying terminologies, and have analyzed SDF models. Takayasu (1982) found SDF behavior in characterizing the complexity of the path of random-walk particles. Using a real-space renormalization argument, Takayasu derived an expression for $D(\lambda)$ for the successive coverage of a one-dimensional random walk with finite mean-free path. Takayasu initially called $D(\lambda)$ a "differential fractal dimension", later using the term "scale-dependent fractal dimension" (Takayasu 1992). Suzuki (1984) found SDF behavior for Japanese coastlines and analyzed a scale-dependent Koch-curve model. Suzuki called $D(\lambda)$ a "transient fractal dimension" and the associated SDFs, "transient fractals". Mark & Aronson (1984) found SDF behavior in the analysis of topographic surfaces and used the term "scale-dependent fractal dimension" for $D(\lambda)$. Chilés (1988) studied fractured rocks and found a continuously-varying "local similarity dimension" as a function of scale. Chilés analyzed several SDF models, including scale-dependent Cantor dust. A smooth variation of the coverage dimension with scale was also found by Miller & Dimotakis (1991a) in their analysis of turbulent-jet scalar data. Rigaut (1991) studied surfaces of biological tissues using microscopic biometry and found SDF behavior. In an analysis of the alveolar structure of lungs of prematurely-born rabbits, Rigaut found a "drifting fractal dimension" with scale and used the term "semi-fractals" for the corresponding SDFs.

In the framework of SDF geometry, the concept of fractal dimension is extended to that of a *scale-dependent-fractal dimension*, $D(\lambda)$, which can be defined as (Takayasu 1982, 1992, Miller & Dimotakis 1991a, Dimotakis 1991)

$$D(\lambda) \equiv -\frac{\mathrm{d}\log N(\lambda)}{\mathrm{d}\log\lambda} \ . \tag{7}$$

The SDF dimension, $D(\lambda)$, is bounded from below by the topological dimension, d_t, and from above by the embedding dimension, d_e, *i.e.*,

$$d_\mathrm{t} \ \leq \ D(\lambda) \ \leq \ d_\mathrm{e} \ . \tag{8}$$

At any given scale, the SDF dimension can approach the topological dimension for the least space-filling sets and the embedding dimension for the most space-filling sets. SDF dimensions, defined through Eq. 7, allow for the description of phenomena whose geometric-scaling laws are scale-dependent, as can be expected to be admissible in general.

The SDF geometric-coverage law that follows from Eq. 7 is given, in differential form, by

$$\frac{\mathrm{d}N(\lambda)}{N(\lambda)} \ = \ -D(\lambda)\frac{\mathrm{d}\lambda}{\lambda} \quad , \tag{9}$$

which shows that the SDF dimension of a set is equal to the fractional decrease in coverage, $-\,\mathrm{d}N/N$, per unit fractional increase in scale, $\mathrm{d}\lambda/\lambda$. We note that, if $D(\lambda) \neq$ const., the SDF differential-coverage relation of Eq. 9 does *not* imply a power-law-like coverage, *i.e.*, $N(\lambda) \not\propto \lambda^{-D(\lambda)}$ (*cf.* Eq. 5). In particular, integrating the differential coverage relation, Eq. 9, from a reference scale, λ_1, to any scale, λ, we see that a SDF dimension implies a geometric-scaling coverage law given by (*cf.* Takayasu 1982, 1992)

$$\frac{N(\lambda)}{N(\lambda_1)} \ = \ \exp\left\{-\int_{\lambda_1}^{\lambda} D(\lambda')\,\frac{\mathrm{d}\lambda'}{\lambda'}\right\} \ = \ \exp\left\{\int_{\lambda}^{\lambda_1} D(\lambda')\,\frac{\mathrm{d}\lambda'}{\lambda'}\right\} \ . \tag{10}$$

Equation 10 should be contrasted with the scale-local and scale-independent relation (Eq. 5) for power-law fractals. For SDFs, the (logarithmic) coverage is a non-linear and non-local function of (logarithmic) scale. Geometric structure across a wide range of scales can contribute to the coverage at any one scale.

A related geometric measure is the coverage fraction, $F(\lambda)$, which is the volume-fill fraction of the set at a scale λ, and can be defined as (Dimotakis 1991),

$$F(\lambda) \equiv \frac{N(\lambda)}{N_{\rm tot}(\lambda)} \equiv N(\lambda) \left(\frac{\lambda}{\delta}\right)^{d_{\rm e}} \quad , \tag{11}$$

where $N_{\rm tot}(\lambda)$ is the total number of boxes of size λ that fill the space in which the set is embedded, and δ is the largest scale of the set. For level sets derived from two-dimensional data, $d_{\rm e} = 2$, and the coverage fraction, $F_2(\lambda)$, can be computed from

$$F_2(\lambda) \equiv N_2(\lambda) \left(\frac{\lambda}{\delta_{\rm r}}\right)^2 \equiv \frac{\lambda^2 N_2(\lambda)}{\lambda_x \lambda_y} \quad , \tag{12}$$

where $\delta_{\rm r}$ is the circumscribing-rectangle-based spatial extent of the data and λ_x and λ_y are as defined in Eq. 3 (*cf.* Eq. A.1).

The logarithmic derivative of $F(\lambda)$ follows from Eqs. 11 and 7, *i.e.*,

$$\frac{{\rm d}\log F(\lambda)}{{\rm d}\log \lambda} = d_{\rm e} - D(\lambda) \quad , \tag{13}$$

so that the behavior of the coverage fraction is characterized by the (complement of the) SDF dimension. Integrating Eq. 13 from a reference scale λ_1 to a scale λ, we can obtain the SDF geometric law for the coverage fraction,

$$\frac{F(\lambda)}{F(\lambda_1)} = \exp\left\{ \int_{\lambda_1}^{\lambda} [d_{\rm e} - D(\lambda')] \frac{{\rm d}\lambda'}{\lambda'} \right\} = \exp\left\{ -\int_{\lambda}^{\lambda_1} [d_{\rm e} - D(\lambda')] \frac{{\rm d}\lambda'}{\lambda'} \right\} . \tag{14}$$

The implications of SDF geometry, as exhibited in Eqs. 13 and 14, are that the degree to which a SDF fills space varies with scale and that geometric behavior across a wide range of scales can contribute to the volume-fill fraction, $F(\lambda)$, at any one scale, λ. While $N(\lambda)$ and $F(\lambda)$ are non-local functions of scale, the SDF dimension, $D(\lambda)$, provides a scale-local measure of the geometry.

SDF analysis of isosurfaces

We have performed a SDF analysis of the scalar isosurfaces by computing two geometric measures: the coverage, $N_2(\lambda)$, and the volume-fill fraction, $F_2(\lambda)$, (*cf.* Eq. 12). The SDF dimension, $D_2(\lambda)$, was computed using Eq. 7. The isosurfaces that were used for the study of these two measures were computed from the scalar-image data using a bilinear-interpolation method. This method removes several difficulties of conventional digital-image contour-identification methods and yields a representation for the interfaces that is particularly suited for the investigation of coverage and coverage-fraction measures. A new method to compute the coverage and coverage fraction was also developed that removes several shortcomings of conventional box-counting methods. This is discussed in the Appendix.

Figure 12 shows the ensemble-averaged, two-dimensional coverage count, $N_2(\lambda)$, as a function of spatial scale, λ, plotted in logarithmic coordinates, for scalar level sets corresponding to three thresholds for $Re \simeq 9.0 \times 10^3$ (*cf.* Fig. 7). The spatial scale, λ, is normalized by the ensemble-averaged threshold-dependent isoscalar spatial extent, $\delta_{\mathrm{r}}(c; Re)$, *cf.* Figs. 10 and 11. The coverage counts for the medium threshold, $c = c_2$, are larger than for $c = c_1$, or $c = c_3$, in accord with the scalar pdf behavior at this Reynolds number (*cf.* Fig. 7). Figure 12 shows that the (logarithmic) coverage count increases with decreasing (logarithmic) scale in a non-linear fashion, implying a SDF isosurface geometry. The SDF dimension, $D_2(\lambda)$, of the level sets of concentration is shown in Fig. 13 computed for the coverage counts of Fig. 12 using Eq. 7. The spatial scale, λ, is again normalized by the ensemble-averaged threshold-dependent spatial extent, $\delta_{\mathrm{r}}(c; Re)$. It is seen that $D_2(\lambda)$ is a function of scale and, in particular, not a constant, increasing continuously with scale, from near unity, at the smallest scales, to 2, at the largest scales. These limiting values of $D_2(\lambda)$ correspond to the topological dimension, $d_{\mathrm{t}} = 1$, and the embedding dimension, $d_{\mathrm{e}} = 2$, of the scalar level sets respectively. The geometric complexity of the isosurfaces, therefore, increases with increasing spatial scale, with a geometric-scaling law that is scale-dependent.

Figure 14 shows the ensemble-averaged coverage fraction, $F_2(\lambda)$, as a function of spatial scale, λ, plotted in logarithmic coordinates, computed from the coverage counts of Fig. 12 using Eq. 11. The (logarithmic) coverage fraction is also seen

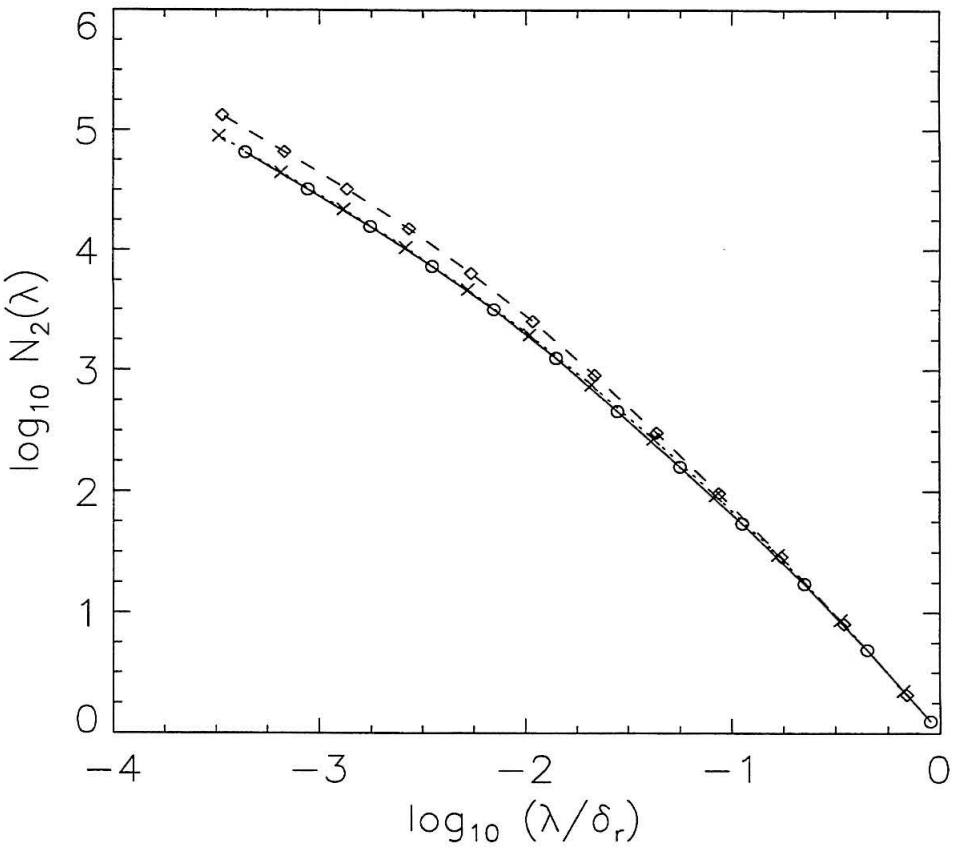

FIG. 12 Coverage, $N_2(\lambda)$, of level sets of mixed-fluid concentration in a turbulent jet at $z/d = 275$ and $Re = 9.0 \times 10^3$, ensemble-averaged from individual-realization coverage counts. Dotted line, crosses: $c = c_1$; dashed line, diamonds: $c = c_2$; solid line, circles: $c = c_3$ (*cf.* Fig. 7).

to increase in a non-linear fashion with increasing (logarithmic) scale (*cf.* Eqs. 13 and 14). The large-scale behavior reflects the highest volume-fill fraction, with $F_2(\lambda) \rightarrow 1$ as $\lambda/\delta_r \rightarrow 1$. The small-scale behavior reflects the lowest volume-fill fraction, with $F_2(\lambda) \rightarrow 0$ as $\lambda/\delta_r \rightarrow 0$. In other words, the volume-fill fraction of the scalar isosurfaces is a SDF function of scale, increasing with scale, with a smooth variation between highest and lowest volume-fill fractions at the largest and smallest scales, respectively (*cf.* Dimotakis 1991).

Our data suggest that the isosurfaces exhibit a SDF geometry throughout the Reynolds-number range investigated in our experiments. Figure 15 shows the SDF

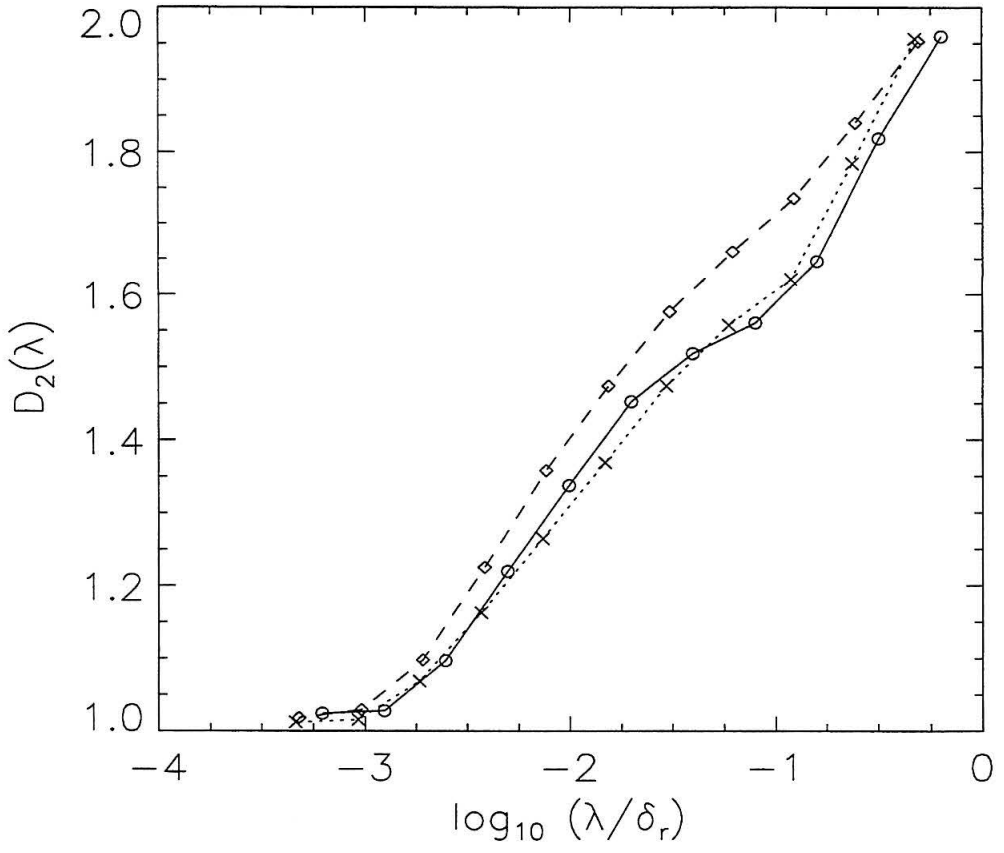

FIG. 13 SDF dimension, $D_2(\lambda)$, of scalar level sets computed from the coverage data of Fig. 12. Dotted line, crosses: $c = c_1$; dashed line, diamonds: $c = c_2$; solid line, circles: $c = c_3$ (*cf.* Fig. 7).

dimension of level sets of concentration for $4.5 \times 10^3 \leq Re \leq 18 \times 10^3$, at the $c = c_1$ threshold corresponding to outer isosurfaces (*cf.* Fig. 7). The larger fluctuations in $D_2(\lambda)$ at larger scales are the result of the relatively lower coverage counts and statistical confidence at those scales compared to the finer scales. At the small scales, *i.e.*, $-3 \lesssim \log_{10}(\lambda/\delta_r) \lesssim -2$, the SDF dimension is seen to increase monotonically with increasing Reynolds number for $4.5 \times 10^3 \leq Re \leq 18 \times 10^3$, indicating that the smaller turbulent-mixing scales become more prevalent with increasing Re. This behavior should be viewed in conjunction with the transition found in the analysis of classical isoscalar measures with increasing Reynolds number (*cf.* Figs. 7, 9, and 11) in the Reynolds-number range investigated in these experiments. Figure 16 shows the volume-fill fraction, $F_2(\lambda)$, of the outer level sets of concentration for

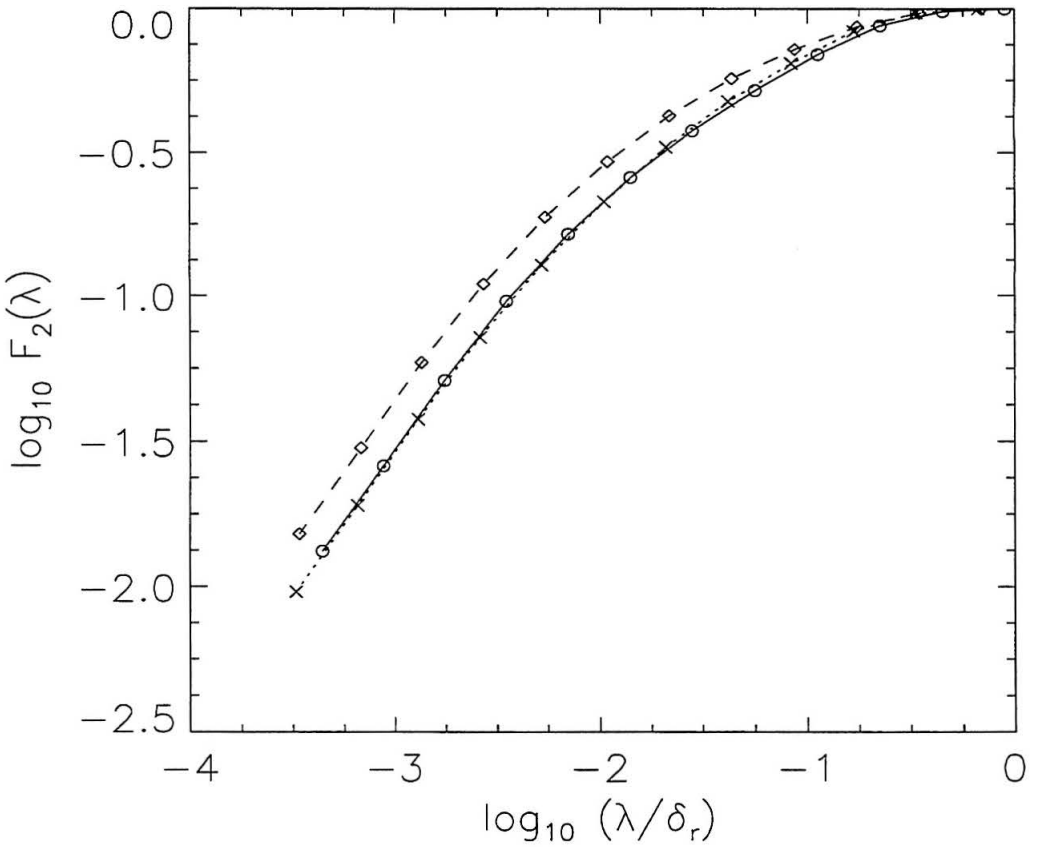

FIG. 14 Volume-fill fraction, $F_2(\lambda)$, of scalar level sets computed from the coverage data of Fig. 12. Dotted line, crosses: $c = c_1$; dashed line, diamonds: $c = c_2$; solid line, circles: $c = c_3$ (*cf.* Fig. 7).

$4.5 \times 10^3 \leq Re \leq 18 \times 10^3$, with $c = c_1$ as the scalar threshold (*cf.* Fig. 7). The Reynolds-number dependence of $F_2(\lambda)$, even at the fine scales, is not evident from Fig. 16, in contrast to the behavior of $D_2(\lambda)$ at the fine scales (*cf.* Fig. 15). The non-local SDF behavior of the level sets implies that fluctuations in $F_2(\lambda)$ at large scales are coupled to the small-scale behavior (*cf.* Eq. 14). The coverage, $N_2(\lambda)$, and the volume-fill fraction, $F_2(\lambda)$, are not scale-local measures of the level-set geometry and, as a result, the behavior of either of these two quantities on a parameter (*e.g.*, Re), at a given scale, is dependent on the behavior at other scales. The logarithmic derivative of $F_2(\lambda)$, on the other hand, is the complement of the SDF dimension (*cf.* Eq. 13). The SDF dimension, $D_2(\lambda)$, does provide a scale-local measure of the level sets. It can be used, therefore, to compare the geometric behavior as a function of

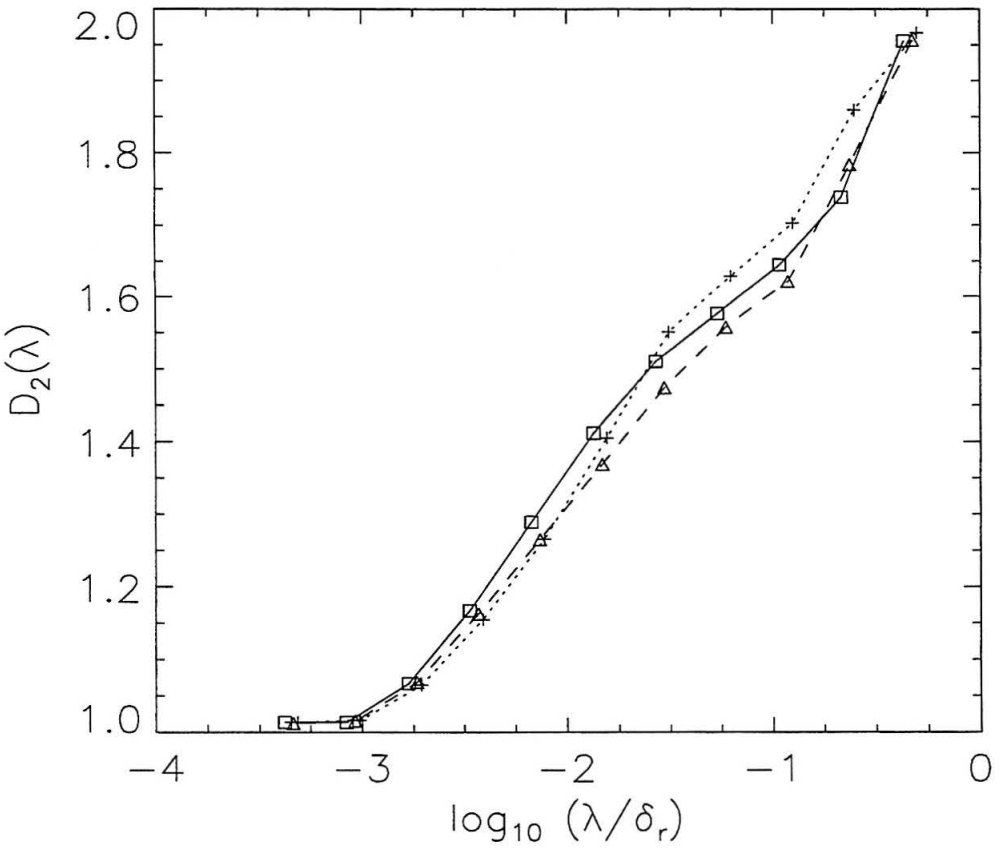

FIG. 15 Reynolds-number dependence of SDF dimension of outer level sets of concentration. Dotted line, crosses: $Re \simeq 4.5 \times 10^3$; dashed line, triangles: $Re \simeq 9.0 \times 10^3$; solid line, squares: $Re \simeq 18 \times 10^3$. The scalar threshold is $c = c_1$ (*cf.* Fig. 7).

a parameter (*e.g.*, Re) at a given scale.

The large range of spatial scales generated by the turbulent-mixing process at the Reynolds numbers of this investigation (*cf.* Figs. 12 and 13) and the exponential dependence of geometric measures on the SDF dimension as, for example, in the SDF relation for the coverage (Eq. 10), imply that assumptions of constant (power-law) fractal dimensions can lead to estimates of geometric measures for the isosurfaces that are substantially different from the actual measures. The notion of SDF dimensions in conjunction with the associated SDFs, provide the necessary framework to accurately characterize complex isosurfaces. From this general frame-

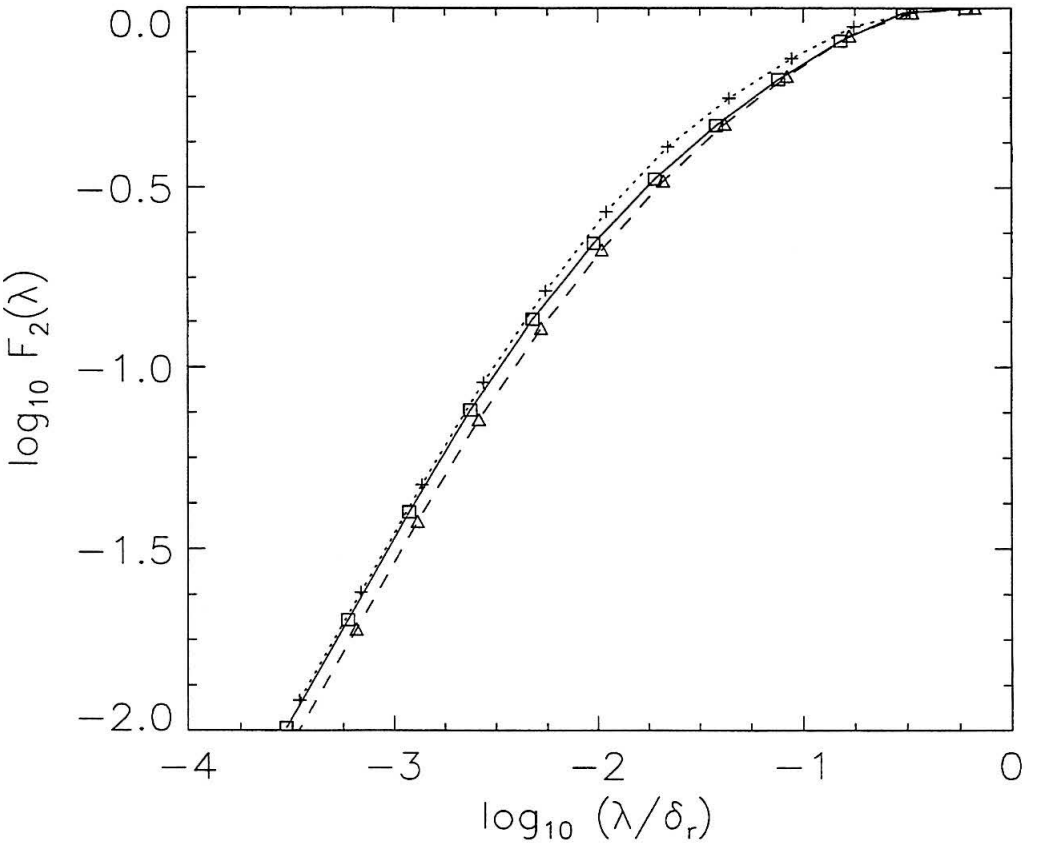

FIG. 16 Reynolds-number dependence of volume-fill fraction of outer level sets of concentration. Dotted line, crosses: $Re \simeq 4.5 \times 10^3$; dashed line, triangles: $Re \simeq 9.0 \times 10^3$; solid line, squares: $Re \simeq 18 \times 10^3$. The scalar threshold is $c = c_1$ (*cf.* Fig. 7).

work, one can expect that (power-law) fractal geometry would be the exception, rather than the rule, *i.e.*, that natural phenomena may be expected to exhibit, in general, SDF properties. Knowledge of the SDF geometry allows the determination of length, area, surface-to-volume ratio, volume-fill fraction and other geometric measures of interest.

Conclusions

Classical as well as fractal measures of scalar isosurfaces derived from experimental investigations in the far field of turbulent jets were found to be functions of both scalar threshold and Reynolds number. Analysis of the isosurface measures indicates a transition between different turbulent-mixing regimes in the Reynolds number range $4.5 \times 10^3 \leq Re \leq 18 \times 10^3$. The scalar pdf and the area enclosed by scalar level sets suggest that Reynolds-number effects on the turbulent-mixing process are largely confined to the outer isosurfaces. The spatial extent of the scalar isosurfaces was found to vary linearly with threshold at the highest Reynolds number of these investigations, indicating an approach to a Reynolds-number-independent spatial extent. The coverage of level sets of concentration in the two-dimensional images was found to possess a scale-dependent-fractal dimension that increases continuously with increasing scale, from near unity, at the smallest scales, to 2, at the largest scales. This scale-dependent-fractal dimension was found to be a weak function of both threshold and Reynolds number. The volume-fill fraction of level sets of concentration was also found to exhibit scale-dependent-fractal behavior, increasing with increasing scale and approaching unity at the largest scales. These findings necessitate a scale-dependent extension of fractals to address the geometry of isosurfaces in turbulent mixing in jets and, probably, in other flows. Other examples of complex geometries in natural phenomena also require this extension.

Acknowledgements

This work was initially supported by AFOSR Grant 90–0304 and GRI Contract 5087–260–1467, and subsequently by AFOSR Grants F49620–92–J–0290 and F49620–94–1–0353. It is part of a larger effort to investigate turbulent mixing in free-shear flows. The informal collaboration with P. Miller, at various stages of these investigations, and the contributions of D. Lang to the experiments are gratefully acknowledged.

APPENDIX

Isosurface representation and coverage

Conventional methods for the representation and coverage of isosurfaces (level sets) derived from digital images are based on the identification of boundary pixels. Figure A.1 shows an outer isosurface (*cf.* Figs. 7 and 8) depicting the conventional boundary pixels and the corresponding field-of-view of the image. The field-of-view is, by design, larger than the local ($z/d = 275$) transverse jet extent. All individual level sets of the measured isosurfaces are thus closed and fully contained within the field-of-view. A selected portion of the isosurface of Fig. A.1, indicated by an arrow, is shown enlarged in Fig. A.2 using conventional boundary pixels. The boundary-outline-pixel representation for this isosurface is shown in Fig. A.3, superimposed on the conventional-boundary-pixel representation. Boundary-outline pixels were devised by P. Miller and are pixels that cover the outline of the boundary pixels. They were used in the 2-D streak-image data analysis of Miller & Dimotakis (1991a). Boundary-outline pixels are offset with respect to the conventional boundary pixels, as shown in Fig. A.3. Figure A.4 shows a small island and a geometrically-identical lake represented using both conventional and boundary-outline pixels. It is seen that the conventional-boundary-pixel-representation counts for this island and lake are substantially different, even though the two isosurfaces are the same. There is, therefore, an inherent asymmetry in the representation of small lakes and islands using conventional boundary pixels. The boundary-outline-pixel representation removes this asymmetry.

Figure A.5 compares the ensemble-averaged coverage counts of outer scalar isosurfaces (*cf.* Fig. 7) represented using both conventional and boundary-outline pixels. The coverage counts for Fig. A.5 were computed using a conventional coverage method in which the field-of-view of the image was successively subdived (*e.g.*, Sreenivasan *et al.* 1989, Miller & Dimotakis 1991a). Figure A.6 shows the corresponding ensemble-averaged SDF dimension, $D_2(\lambda)$. It is seen that the conventional boundary-pixel representation can lead to $D_2(\lambda)$ values at the smallest scales that are less than the topological dimension, d_t, *i.e.*, unity, in this case,

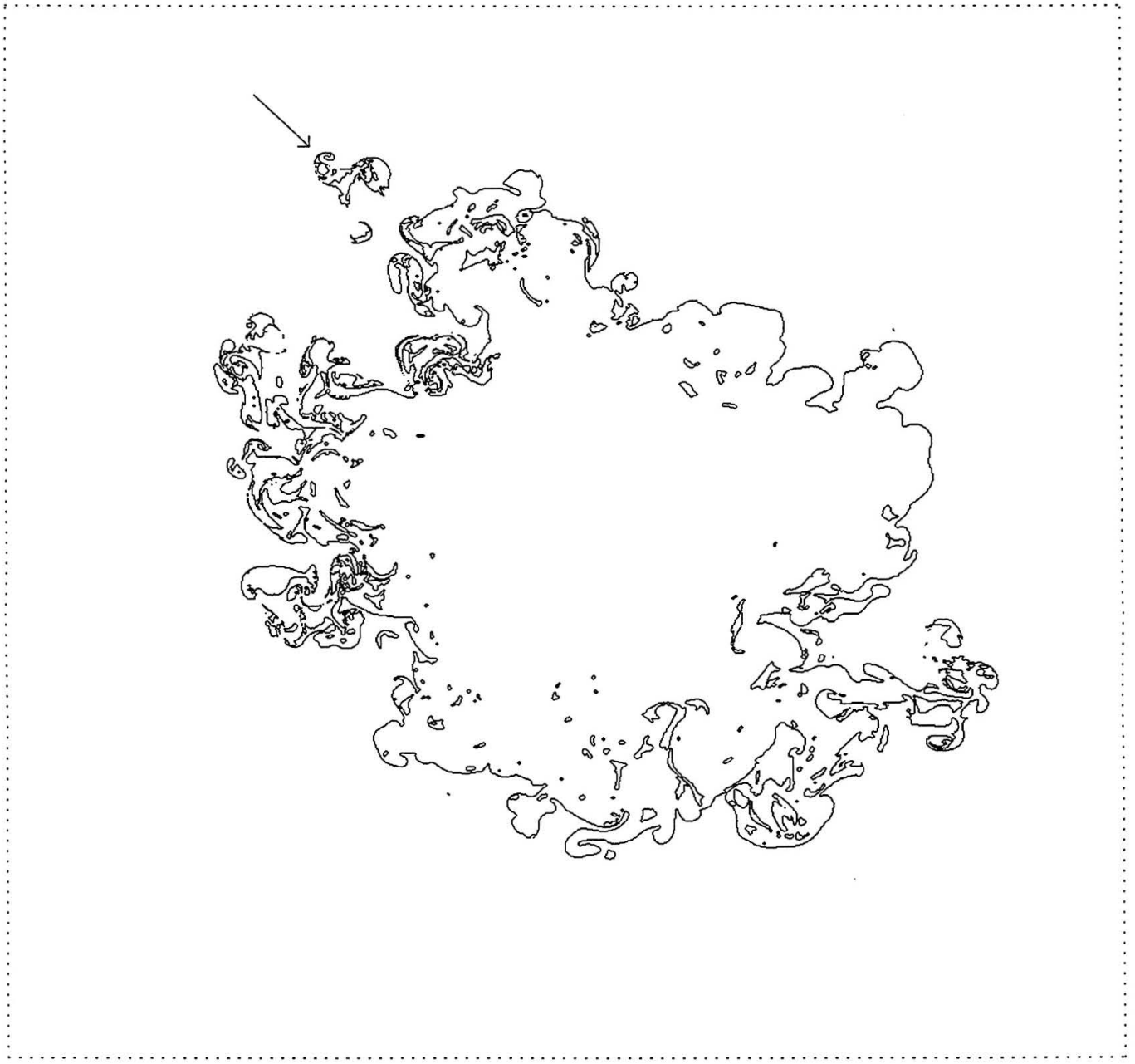

FIG. A.1 Outer scalar isosurface for $c = c_1$ at $Re = 9.0 \times 10^3$ (*cf.* Fig. 7) depicted using conventional boundary pixels. Also shown is the field-of-view (dotted line). Arrow indicates a scalar island, magnified and shown in Fig. A.2.

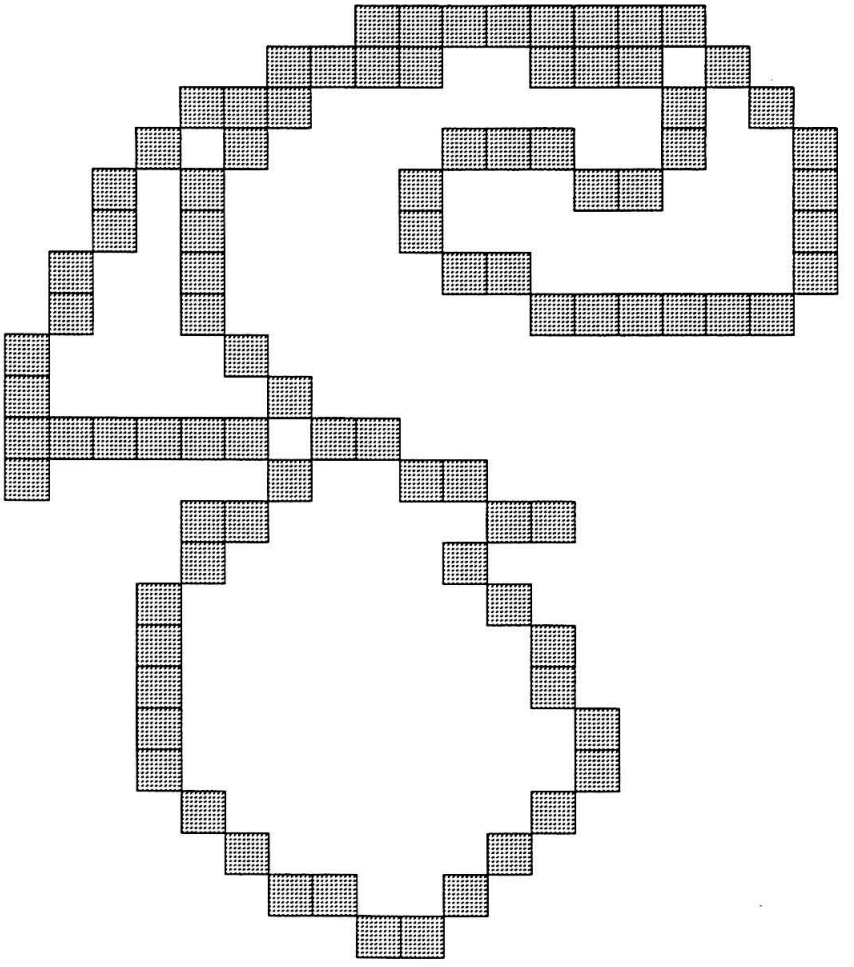

FIG. A.2 Representation of a scalar island belonging to an outer isosurface (*cf.* Fig. A.1) using conventional boundary pixels (shaded squares).

violating the range constraint on $D(\lambda)$ (Eq. 8). This is a result of the asymmetry inherent in conventional boundary-pixel representations, as noted above. The

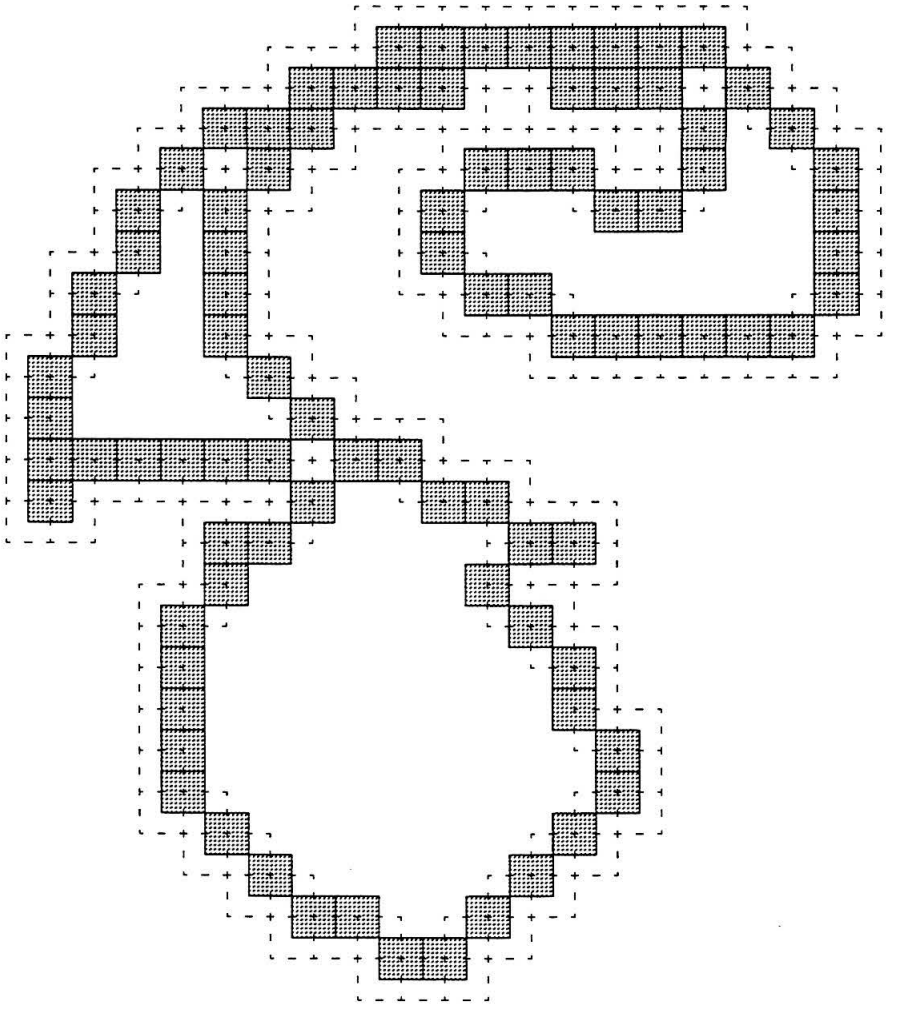

FIG. A.3 Representation of the scalar island of Fig. A.2 using boundary-outline pixels (dashed line), superimposed on the conventional boundary pixels (shaded squares).

boundary-outline-pixel representation removes this problem as shown in Fig. A.6.

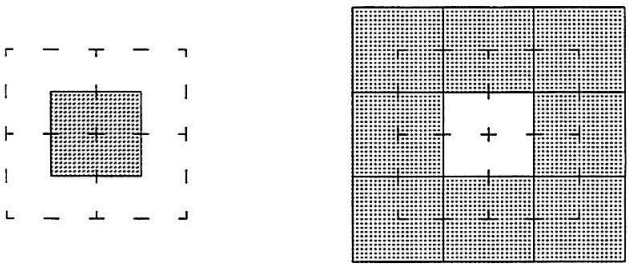

FIG. A.4 Demonstration of asymmetry inherent in conventional-boundary-pixel representations. A small island (left) is shown represented using conventional boundary pixels (shaded squares) and boundary-outline pixels (dashed line). A geometrically-identical lake (right) is also shown using both representations.

The coverage results of Fig. A.5, however, exhibit an inflection point at large scales for both representations. This is manifested as a dip in the value of $D_2(\lambda)$ at the large scales, as seen in the SDF dimension results in Fig. A.6. This is an artifact of the fact that the conventional box-counting methods employed to produce the data in Fig. A.6 subdivide the field-of-view of the image. Those methods do not account for the finite spatial extent of the data and, as a result, do not produce minimum coverage counts. Such methods can mask the coverage behavior of the data at the outer scales, producing counts that substantially overestimate the minimum coverage counts at those scales. For example, the ensemble-averaged coverage counts based on successive subdivision of a larger field-of-view (2048×2048 square-pixels) are also shown in Figs. A.5 and A.6. It is seen that a larger field-of-view, for the same data, can influence the large-scale estimate of the SDF dimension.

To address these issues, we have developed a modified box-counting method, the Rectangular Coverage Method, that removes several shortcomings of conven-

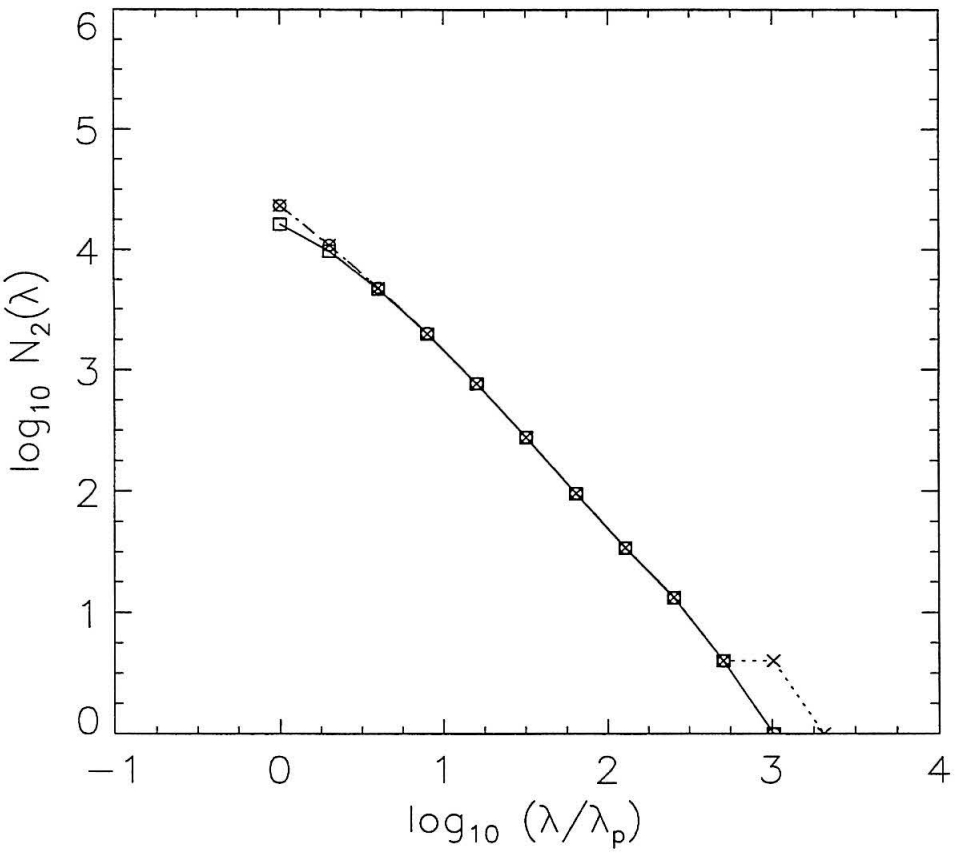

FIG. A.5 Ensemble-averaged coverage counts, $N_2(\lambda)$, of scalar level sets for $c = c_1$, at $Re = 9.0 \times 10^3$ (*cf.* Fig. 7), computed by successive subdivision of the field-of-view (*cf.* Fig. A.1). Solid line, squares: conventional boundary pixels; dashed line, circles: boundary-outline pixels. Also shown are the ensemble-averaged coverage counts computed by successive subdivision of a larger field-of-view (2048 × 2048 square-pixels) for the same isosurfaces represented using boundary-outline pixels (dotted line, crosses).

tional box-counting methods. The modified method accounts for the finite spatial extent of each particular isosurface and is able to produce near-minimum coverage counts over the whole range of scales, from the image-pixel resolution to the spatial extent. The first step of the method is to estimate the spatial extent of each particular isosurface. This is achieved by identifying the smallest circumscribing rectangle (*cf.* Tricot 1995) that covers the isosurface. Figure A.7 shows an example of a circumscribing rectangle computed for the isosurface of Fig. A.1, as well as the extent of the image field-of-view. A coverage count of unity is assigned for the

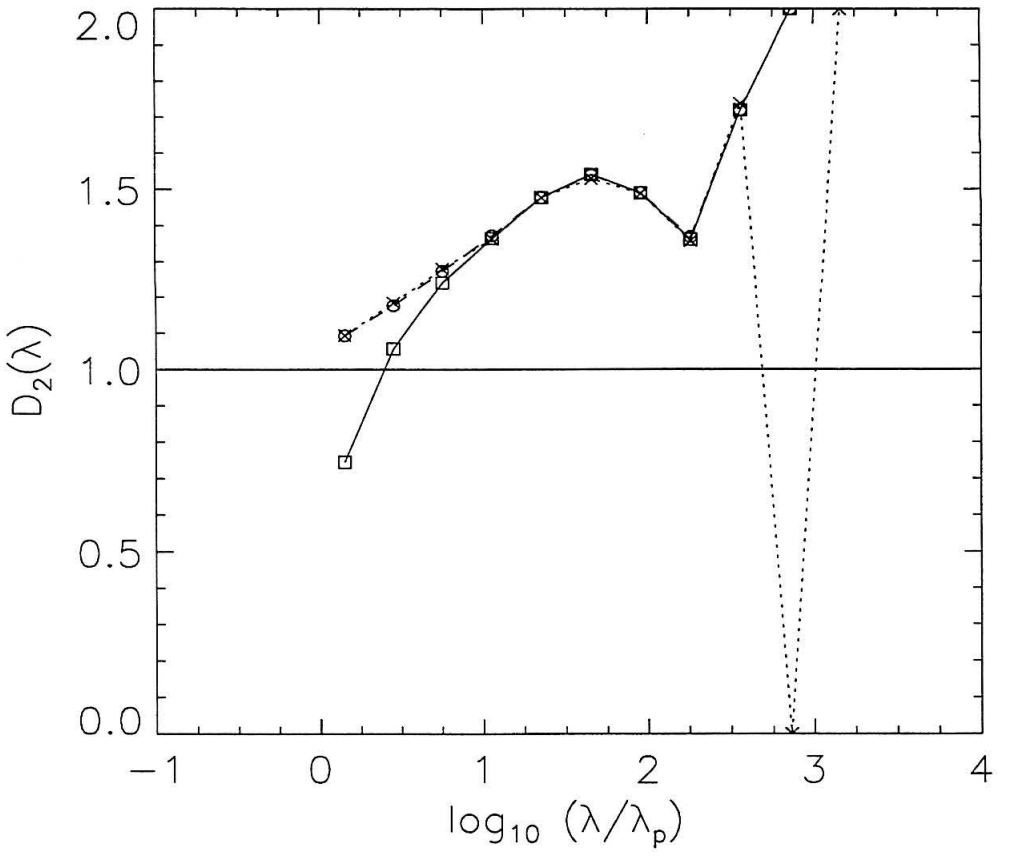

FIG. A.6 Comparison of SDF dimension, $D_2(\lambda)$, computed for the coverage counts of Fig. A.5. Same legend as Fig. A.5. The topological dimension, $d_t = 1$, is also shown (solid line).

circumscribing rectangle. The single scale that corresponds to this coverage count is assigned to the *geometric mean* of the lengths of the two sides, λ_x and λ_y, of the circumscribing rectangle. This scale is also taken as an estimate of the spatial extent, δ_r, of the isosurface, *i.e.*,

$$\delta_r \equiv (\lambda_x \lambda_y)^{1/2} \quad , \tag{A.1}$$

and

$$N_2(\delta_r) = 1 \ . \tag{A.2}$$

The circumscribing rectangle is subdivided into four equal rectangles, and the number of the smaller rectangles covering parts of the isosurface is counted. The associated λ-scale corresponding to this count is computed, in a similar fashion, as the

geometric mean of the sides of the smaller rectangles. The process is repeated by further subdividing each rectangle.

We have also developed an improved representation method for the isosurfaces. We note that boundary-pixel-based representations have the limitation that the smallest scale at which the isosurface can be represented is limited by the pixel scale. Also, in conventional methods, portions of the isosurface that lie at 45° to the image axes result in step-like representations. In the present study, we have chosen to represent the isosurfaces using bilinear interpolation. Bilinear interpolation conserves the integral under the scalar surface. The constraint that the scalar surface $c(\mathbf{x})$ be smooth and the requirement that the integral under the scalar surface match the particular pixel output is enough to specify the actual surface, and thus locate the isosurfaces. Figure A.8 shows the bilinearly-interpolated representation (solid line) of an isosurface (*cf.* Fig. A.3). For every set of four neighbouring image pixels, a piece of the isosurface is computed using bilinear interpolation. Bilinear interpolation can, in general, give two branches within any four-pixel region, each of which belongs to a different isosurface. For this reason, a contour-following algorithm was written which marches along the boundary pixels belonging to the same isosurface. The resulting curve, *e.g.*, Fig. A.8, is piece-wise bilinear and closed.

The ensemble-averaged coverage computed using the Rectangular Coverage Method applied to bilinearly-interpolated isosurfaces is shown in Fig. A.9 for outer isosurfaces (*cf.* Fig. 7). For comparison purposes, Fig. A.9 also shows the coverage counts computed using the Rectangular Coverage Method for isosurfaces represented using boundary-outline pixels, as well as the coverage counts computed using the conventional, field-of-view-based, box-counting method applied to boundary-outline pixels. Figure A.10 shows the ensemble-averaged SDF dimensions corresponding to the coverage counts of Fig. A.9. It is seen that the Rectangular Coverage Method removes the (artificial) dip in the value of $D_2(\lambda)$ at large scales associated with conventional box-counting methods. The proposed coverage method yields coverage counts at large scales that follow the actual spatial extent of the isosurfaces. It is noted, additionally, that the coverage counts of the proposed method at small scales agree with the coverage counts obtained using the conventional method at those scales. Figures A.9 and A.10 also show that the bilinear representation yields

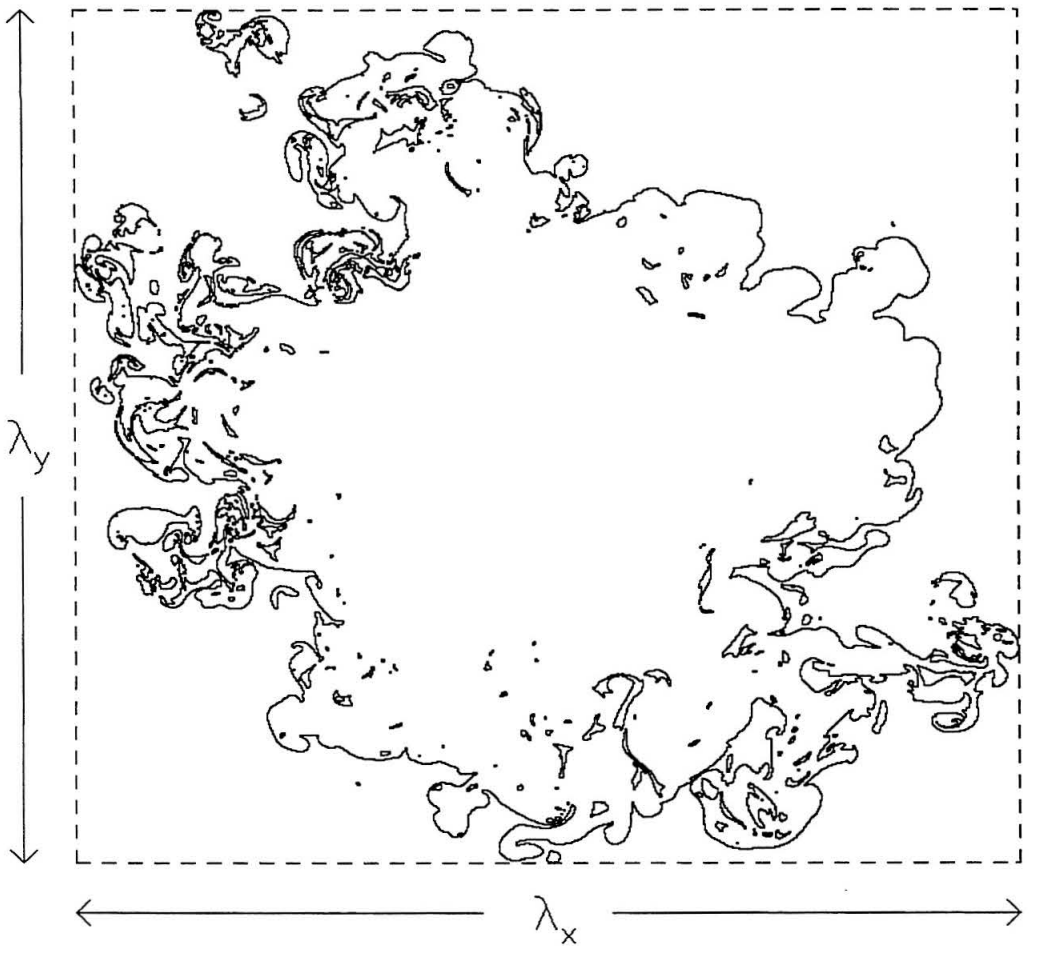

FIG. A.7 Circumscribing rectangle (dashed line) computed for the isosurface of Fig. A.1. Also shown is the field-of-view extent (dotted line). This isosurface is depicted using boundary-outline pixels.

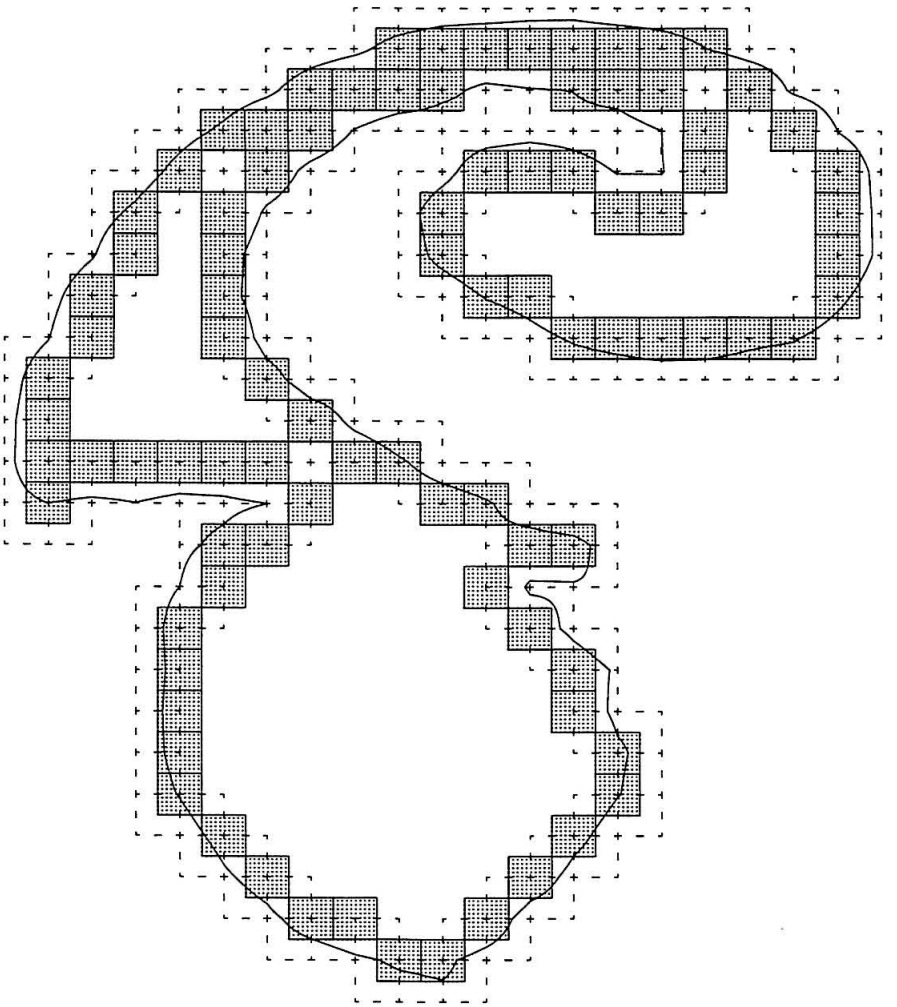

FIG. A.8 Bilinearly-interpolated representation (solid line) of a scalar island (indicated by arrow in Fig. A.1) superimposed on the conventional-boundary-pixel representation (*cf.* Fig. A.2) and the outline-boundary-pixel representation (*cf.* Fig. A.3).

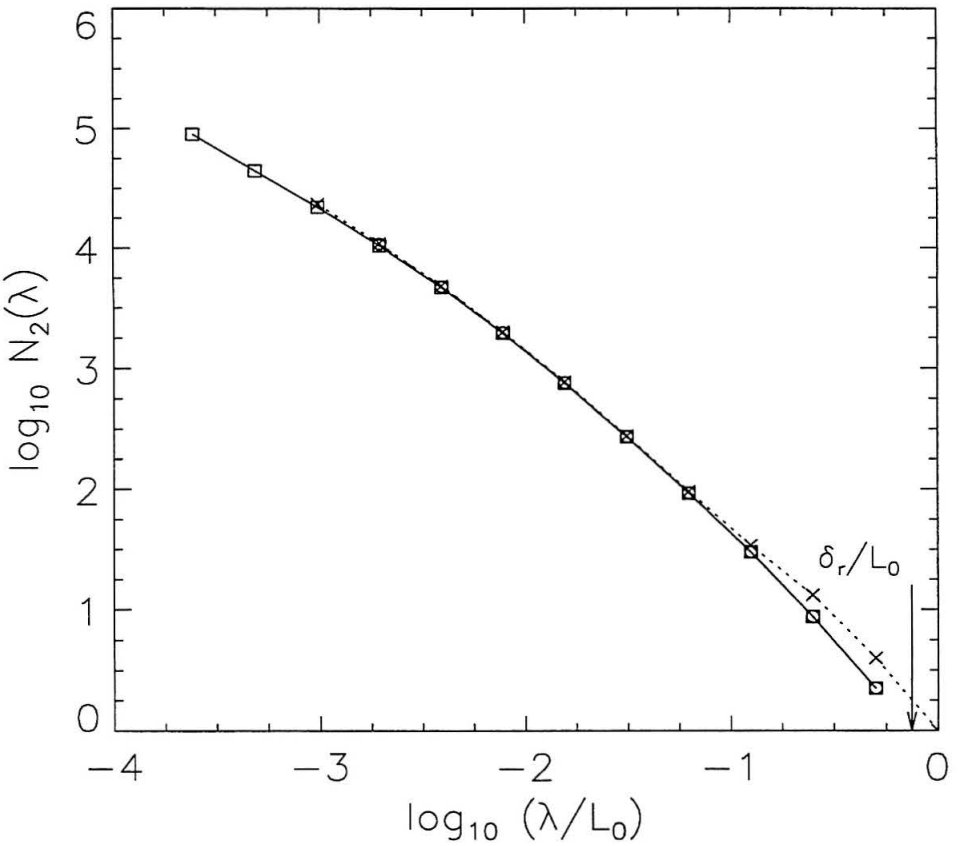

FIG. A.9 Ensemble-averaged coverage counts, $N_2(\lambda)$, of scalar level sets for $c = c_1$, at $Re = 9.0 \times 10^3$ (*cf.* Fig. 7), computed using the Rectangular Coverage Method for level sets represented using bilinear interpolation (solid line, squares) and boundary-outline pixels (dashed line, circles). Dotted line, crosses: conventional, field-of-view-based coverage counts using boundary-outline pixels (*cf.* Fig. A.5).

coverage counts which agree, at the large scales, with the counts obtained using boundary-outline-pixel representations. At the small scales, boundary-outline-pixel representations lead to overestimates of the coverage necessary for the isosurfaces. Also, the smallest scale at which the conventional methods can produce coverage counts is limited by the pixel scale. The bilinear-interpolation representation, as seen in Fig. A.10, leads to coverage results that do not have this limitation. The SDF dimension approaches unity asymptotically at the smallest scales, as expected. In addition, as seen in Fig. A.10, bilinear interpolation allows a more accurate esti-

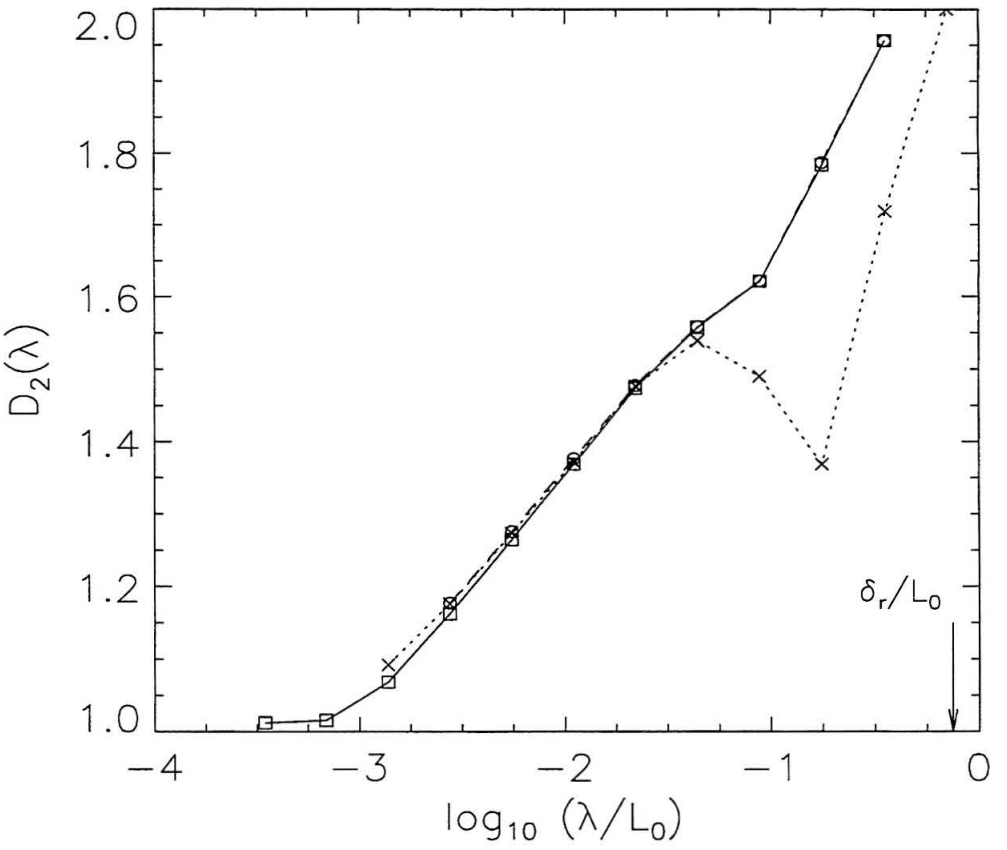

FIG. A.10 Comparison of SDF dimension, $D_2(\lambda)$, computed for the coverage counts of Fig. A.9. Same legend as Fig. A.9.

mate of the coverage behavior at scales in the neighborhood of the pixel resolution, as compared to conventional representation methods.

References

BAUMANN, G., BARTH, A. & NONNENMACHER, T. F. 1994 "Measuring Fractal Dimensions of Cell Contours: Practical Approaches and their Limitations," in *Fractals in Biology and Medicine* (T. F. Nonnenmacher, G. A. Losa, E. R. Weibel, Eds., Birkhäuser-Verlag, Basel, Switzerland), 182–189.

CHILÉS, J. P. 1988 "Fractal and Geostatistical Methods for Modeling of a Fracture Network," *Math. Geol.* **20**(6), 631–654.

CONSTANTIN, P. 1989 "Remarks on the Navier-Stokes equations," in *New Perspectives in Turbulence* (L. Sirovich, Ed., Springer-Verlag, NY, 1991), 229–261.

CONSTANTIN, P. 1990 "Navier-Stokes Equations and Area of Interfaces," *Comm. Math. Phys.* **129**, 241–266.

CONSTANTIN, P. 1994a "Geometric Statistics in Turbulence," *SIAM Rev.* **36**(1), 73–98.

CONSTANTIN, P. 1994b "Geometric and Analytic Studies in Turbulence," in *Trends and Perspectives in Applied Mathematics* (L. Sirovich, Ed., Springer-Verlag, NY), 21–54.

CONSTANTIN, P. & PROCACCIA, I. 1994 "The geometry of turbulent advection: sharp estimates for the dimensions of level sets," *Nonlinearity* **7**, 1045–1054.

CONSTANTIN, P., PROCACCIA, I. & SREENIVASAN, K. R. 1991 "Fractal Geometry of Isoscalar Surfaces in Turbulence: Theory and Experiment," *Phys. Rev. Lett.* **67**(13), 1739–1742.

DIMOTAKIS, P. E. 1991 "Fractals, dimensional analysis and similarity, and turbulence," *Nonlinear Sci. Today* #2/91, pp. 1, 27–31.

DIMOTAKIS, P. E. 1993 "Some issues on turbulent mixing and turbulence," GALCIT Report FM93–1a.

DIMOTAKIS, P. E., MIAKE-LYE, R. C. & PAPANTONIOU, D. A. 1983 "Structure and Dynamics of Round Turbulent Jets," *Phys. Fluids* **26**, 3185–3192.

FALCONER,K. J. 1990 *Fractal Geometry: Mathematical Foundations and Applications* (Wiley, Chichester).

FLOHR, P. & OLIVARI, D. 1994 "Fractal and multifractal characteristics of a scalar dispersed in a turbulent jet," *Physica D* **76**, 278–290.

GLUCKMAN, B. J., WILLAIME, H. & GOLLUB, J. P. 1993 "Geometry of isothermal and isoconcentration surfaces in thermal turbulence," *Phys. Fluids* **5**(3), 647–661.

KERSTEIN, A. R. 1991 "Linear-eddy modeling of turbulent transport. Part V: Geometry of scalar interfaces," *Phys. Fluids* A **3**(5), Pt. 2, 1110–1114.

LANE–SERFF, G. F. 1993 "Investigation of the fractal structure of jets and plumes," *J. Fluid Mech.* **249**, 521–534.

MANDELBROT, B. B. 1967 "How long is the coast of Britain? Statistical self-similarity and fractional dimension," *Science* **155**, 636–638.

MANDELBROT, B. B. 1975a "On the geometry of homogeneous turbulence, with stress on the fractal dimension of the iso-surfaces of scalars," *J. Fluid Mech.* **72**(2), 401–416.

MANDELBROT, B. B. 1975b *Les objets fractals: forme, hasard et dimension* (Flammarion, Paris).

MANDELBROT, B. B. 1977 *Fractals. Form, Chance, and Dimension* (W. H. Freeman, San Francisco).

MANDELBROT, B. B. 1983 *The Fractal Geometry of Nature* (W. H. Freeman, New York).

MANDELBROT, B. B. 1989 "Fractal geometry: What is it and what does it do?," in *Fractals in the Natural Sciences* (M. Fleischmann, D. J. Tildesley, R. C. Ball, Eds., Princeton), 7.

MARK, D. M. & ARONSON, P. B. 1984 "Scale-Dependent Fractal Dimensions of Topographic Surfaces: An Empirical Investigation, with Applications in Geomorphology and Computer Mapping," *Math. Geol.* **16**(7), 671–683.

MCCOMB, W. D. 1991 *The physics of fluid turbulence* (Clarendon Press, Oxford).

MIKHAILOV, A. S. & LOSKUTOV, A. Y. 1991 *Foundations of Synergetics* **II**: *Complex Patterns* (Springer-Verlag, Berlin).

MILLER, P. L. & DIMOTAKIS, P. E. 1991a "Stochastic geometric properties of scalar interfaces in turbulent jets," *Phys. Fluids A* **3**, 168–177.

MILLER, P. L. & DIMOTAKIS, P. E. 1991b "Reynolds number dependence of scalar fluctuations in a high Schmidt number turbulent jet," *Phys. Fluids A* **3**, 1156–1163.

PRASAD, R. R. & SREENIVASAN, K. R. 1990 "Quantitative three-dimensional imaging and the structure of passive scalar fields in fully turbulent flows," *J. Fluid Mech.* **216**, 1–34.

PROCACCIA, I., BRANDENBURG, A., JENSEN, M. H. & VINCENT, A. 1992 "The fractal dimension of isovorticity structures in 3-dimensional turbulence," *Europhys. Lett.* **19** (3), 183–187.

RICHARDSON, L. F. 1961 "The problem of contiguity: an appendix of statistics of deadly quarrels," *General Systems Yearbook* **6**, 139–187.

RIGAUT, J.-P. 1991 "Fractals, semi-fractals, and biometry," in *Fractals: Non-integral Dimensions and Applications* (G. Cherbit, Ed., Wiley, Chichester, UK), 151–187.

SREENIVASAN, K. R. 1991 "Fractals and Multifractals in Fluid Turbulence," *Ann. Rev. Fluid Mech.* **23**, 539–600.

SREENIVASAN, K. R. 1994 "Fractals in Fluid Mechanics," *Fractals* **2** (2), 253–263.

SREENIVASAN, K. R. & MENEVEAU, C. 1986 "The Fractal Facets of Turbulence," *J. Fluid Mech.* **173**, 357–386.

SREENIVASAN, K. R., PRASAD, R. R., MENEVEAU, C. & RAMSHANKAR, R. 1989 "The Fractal Geometry of Interfaces and the Multifractal Distribution of Dissipation in Fully Turbulent Flows," *Pure & Appl. Geoph.* **131**(1–2), 43–60.

SUZUKI, M. 1984 "Finite-Size Scaling for Transient Similarity and Fractals," *Prog. Theor. Phys.* **71**(6), 1397–1400.

TAKAYASU, H. 1982 "Differential Fractal Dimension of Random Walk and Its Applications to Physical Systems," *J. Phys. Soc. Japan* **51**(9), 3057–3064.

TAKAYASU, H. 1992 *Fractals in the Physical Sciences* (Wiley, Chichester, UK).

TAYLOR, G. I. 1920 "Diffusion by Continuous Movements," *Proc. London Math. Soc.* **20**, 196–212.

TRICOT, C. 1995 *Curves and Fractal Dimension* (Springer-Verlag, New York).

VICSEK,T. 1992 *Fractal Growth Phenomena* (2nd Ed., World Scientific, Singapore).

VINCENT, A. & MENEGUZZI, M. 1991 "The spatial structure and statistical properties of homogeneous turbulence," *J. Fluid Mech.* **225**, 1–20.